Zagazig University Medical Journal
www.zumj.journals.ekb.eg

https://doi.org/10.21608/zumj.2024.319646.3575 Volume 31, Issue 1, January. 2025

Manuscript id: ZUMJ-2409-3575
Doi: 10.21608/ZUMJ.2024.319646.3575

ORIGINAL ARTICLE

Possible Effects of Empagliflozin on Hippocampal Structural Changes Associated with Alzheimer's disease Induced by Aluminum Chloride in Adult Male Albino Rats (Histological and Immunohistochemically Study)

Mohamed Abdel AL-Rahman Shaheen[1], Laila Mostafa ELshal[1], Gehad Magdy Mohamed[1], Samar Mohamed Reda[1*]

[1]Medical Histology Department, Faculty of Medicine, Zagazig University, Zagazig, Egypt.

***corresponding author:**
Samar Mohamed Reda
E mail:
drsamrreda@yahoo.com

Submit Date: 12-09-2024
Revise Date: 06-10-2024
Accept Date: 09-10-2024

ABSTRACT

Background: Alzheimer's disease (AD) is a prevalent neurological condition that worsens over time. Inadequate therapy causes AD to worsen more quickly. Therefore, our goals were to show the detrimental effects of AD caused by Aluminum chloride (ALCL3) on the adult male albino rat hippocampal structure, as well as to elucidate any potential benefits of empagliflozin (EMP) in reversing these structural alterations.

Methods: Thirty-six adult male albino rats were randomly divided into three main groups: Group (I)was the control group, group (II) (Alzheimer-induced model group) was given aluminum chloride dissolved in distilled water (100mg/kg/day) orally for 8 weeks and Group (III) EMP-treated groups Ameliorative group (IIIa): was given EMP dissolved in distilled water, at a dose of (3mg/kg/day) orally concomitant with aluminum chloride at the same dose and for the same period of the previous group. and Curative group (IIIb) Rats received ALCL3 (100mg/Kg/body weight) for 8 weeks and were subsequently treated by EMP (3 mg/Kg) for another week dissolved in distilled water, which was given by oral gavage.

Results: There was a statistically significant decrease in T-maze and TAC in the curative compared to the control group and ameliorative group ($p<0.05$), while there was a statistically significant increase in Malondialdehyde(MDA) in the curative compared to the control group and ameliorative group. The Alzheimer-induced model group showed structural changes in the Cornu Ammonis 1(CA1) and Dentate gyrus (DG) in the form of distortion of pyramidal cells, disturbed granular cell layer, and that they appeared with darkly stained pyknotic nuclei. Intense positive immunoreaction for GFAP in the cytoplasm and processes of astrocytes were observed. A marked decrease in the immunoreactivity for SYP on the surface of the pyramidal cell and granular cell bodies with their apical dendrites of CA1 and DG of the hippocampus. The ultra-structural study exhibited neurons with apoptotic features and heterochromatic nuclei, and their cytoplasm contained dilated cisternae of rough endoplasmic reticulum and swollen mitochondria. Empagliflozin administration ameliorated these histological and immunohistochemical alterations to a better degree than in the curative group.

Conclusion: AD induced by aluminum chloride resulted in biochemical and histological degenerative changes in the hippocampus CA1 and DG, and the administration of EMP could ameliorate this degenerative damage. Early management with EMP may exert a more highly ameliorative role than late curative.

Keywords: Empagliflozin, Alzheimer's disease, Aluminum chloride, Rats.

INTRODUCTION

The prevalent chronic neurological disease known as Alzheimer's disease (AD) is brought on by structural and functional abnormalities in the brain. For the majority of dementia cases, it is the primary cause. Around 50 million people worldwide suffer from AD, and due to a lack of precise diagnosis and treatment, it is expected that this figure will rise to 130 million by 2050 [1]. Target therapy comes in a variety of forms; however, treating AD is challenging due to its intricate and multifaceted etiology. The pathogenesis of AD is explained by a number of theories, including the βeta-amyloid (Aβ) cascade, tau proteinopathy, cholinergic hypothesis, increased oxidative stress, and neuroinflammatory. AD risk is increased by additional factors. One major risk factor for the onset and prevalence of AD is aging. Since AD degeneration is noticeably worse than that of normal aging and cannot be distinguished, AD is regarded as a public health concern [2]. Amyloid plaques and neurofibrillary tangles are the two main abnormal brain occurrences linked to Alzheimer's disease. Amyloid plaques, which cause degeneration of neurons and other nerve cells, are aberrant aggregates of the protein beta-amyloid that are found extracellularly in the tissue separating nerve cells. Tau protein abnormally accumulates inside neurons to form neurofibrillary tangles (NFTs). Tau typically attaches to and stabilizes microtubules in healthy neurons. Twisted filament bundles, which are threads and tangles inside neurons, are formed when Tau detaches from microtubules and sticks to generate other tau molecules in AD due to an aberrant chemical shift. Microtubule malfunction that results from the formation of NFTs blocks synaptic transmission and the brain transport system [3].

The medial temporal lobe's hippocampus is a neuronal structure that has a distinctive C-shaped curvature. One important part of the limbic system is the hippocampal region. It is made up of the dentate gyrus (DG) and the CA1, CA2, CA3, and CA4 regions of Cornu Ammonis. It is a crucial area for memory and learning. The primary cell layer, the deep polymorph layer, and the superficial or molecular layer make up the three layers of the cortex. Declarative and episodic memory developments are issues that the hippocampal region handles. Thus, it is among the areas of the brain impacted by AD [4].

Aluminum chloride (ALCL3) has been routinely utilized to cause dementia in a number of animal models. Aluminum is a neurotoxic element that has been connected to the aberrant emergence of a number of neurological conditions. Excessive quantities of Al were found in post-mortem brain tissue from AD patients, supporting the link between Al exposure and the disease [3].

Gliflozins, which include Empagliflozin, Canagliflozin, and Dapagliflozin, among others, are inhibitors of the sodium-glucose cotransporter-2 (SGLT2). When used to treat people with type 2 diabetes, they are successful [5].

Numerous investigations confirmed the pleiotropic advantages of gliflozin agents. Among the inhibitors of sodium-glucose cotransporter-2 (SGLT2) is empagliflozin (EMP). This drug is antihyperglycemic. Agents known as gliflozins are lipid-soluble, have the ability to pass the blood-brain barrier and have receptors in the central nervous system (CNS) [6]. Empagliflozin has been shown to have a neuroprotective impact on a variety of neurological conditions, including epilepsy and AD. It can lessen the cognitive damage brought on by diabetes (DM). In a rat model, EMP lessens cerebral ischemia/reperfusion injury [7].

METHODS

The experimental protocol was performed in accordance with National Institute of Health (NIH) guidelines for the Care and Use of Laboratory Animals (No. ZU-IACUC/3/F/98/2022).

Materials:

Animals

This study was carried out on thirty-six adult healthy male albino rats (12-14 weeks) weighing 180-220 gm. The animals were supplied by the Laboratory Animal Unit, Faculty of Medicine, Zagazig University. All rats received human care in compliance with the Ethical Committee of Zagazig University and in accordance with the NIH Guidelines for the Care and Use of Laboratory Animals (No. ZU-IACUC/3/F/98/2022).

The rats were given standard, balanced food and unlimited access to water while being housed in carefully monitored settings at room temperature. Three major groups were randomly selected from them:

- **Group I (control):** including 18 rats equally divided into three subgroups (n=6)

Subgroup Ia (negative control): received no treatment**.**

Subgroup Ib (positive control): received distilled water by oral gavage for 8 weeks.

Subgroup Ic (positive control): received the empagliflozin drug by oral gavage at a dose (3 mg/Kg) for 8 weeks **[8].**

- **Group II (Alzheimer-induced model group)**

Including six rats who received oral gavage of dissolved aluminum chloride powder (100 mg/kg/body weight) for eight weeks (1gm from ALCL3 powder dissolved in 10 ml distilled water) **[9].**

- **Group III (Empagliflozin-treated group):**12 rats equally divided into 2 subgroups (n=6):

Subgroup IIIa :(ameliorative group)

Rats given EMP (3 mg/kg) dissolved in distilled water for eight weeks **[8],** which was administered orally along with 100 mg/kg of body weight of aluminum chloride every day for eight weeks **[9].**

Subgroup IIIb :(curative group)

For eight weeks, rats were given 100 mg/kg of body weight of aluminum chloride. **[9]**, and after that received oral gavage treatment with EMP (3 mg/Kg) for 8 weeks after it was dissolved in distilled water **[8].**

The rats' food consumption was monitored during the trial. Rat mortalities were documented; two deaths were seen in the curative group, and three deaths were seen in the AD-induced group.

Methods

Evaluation of Behavioral parameter:

Modified T-maze Test: was conducted at Zagazig University's Faculty of Medicine's Physiology Department. The T-shaped, black, hardwood apparatus that makes up the T-maze apparatus has two goal arms and a central divider, as well as one start arm.

Procedure:

Since the novelty of the maze encourages spontaneous exploration, there is no need for habituation to the maze. The easiest way to estimate the performance is to determine how long it takes an animal in the start area to meet the chosen criterion (whole body plus tail tip on goal arm). A stopwatch can be used to measure this. Sample run: all of the guillotine doors were raised, the central divider was in place, and the maze was assembled. At the beginning of every run, each rat was placed in the start region (bottom of the "T"), and it was allowed to select the goal arm. The rat was gently removed and placed back in the cage for a 10-minute inter-trial period after it had been confined for 30 seconds—regardless of its direction—by softly sliding the door down. Choice runs: the sample run's guillotine door was lifted once more after the central divider was removed. In order to prevent olfactory bias and preserve the animal's interest, a fresh woodchip was placed on the floor for every trial, resulting in a different smell. In the start area, a new rat was inserted and given the option to select one of the two open goal arms. Every trial lasted one to two minutes. When the rat enters the opposite arm from where it entered in the previous run, it is known as alternation. Over the course of two days, one sample and five choice runs were conducted for every rat, for a total of 12 trials per rat and a total of 10 potential alternations **[10].**

- Result analysis: proportion correct choice (alternation) per rat was calculated as follows:

$$\frac{number\ of\ correctchioces(alternations)}{total\ possiple\ alternations} \times 100$$

Animals were put to sleep 24 hours after the trial ended with an intraperitoneal injection of 50 mg/kg body weight of thiopental [11]. Blood samples were taken from the orbital vein when they were fully unconscious in order to estimate their blood glucose levels. Next, each animal's cranium vault was quickly removed, exposing the cerebral cortex and remnants of the meninges. The brain was rapidly removed, with its two cerebral hemispheres processed for examination under an electron and light microscope. A cold phosphate buffer was used to homogenize additional hemispheres in order to assess the oxidative stress indicators.

Biochemical study:

All rats had venous blood (4 ml) extracted via retro orbital puncture and placed in centrifuge tubes. After allowing the samples to clot, the serum was separated by centrifuging them at a speed of 3000 rounds per minute. They were kept at a temperature of -20°C in a freezer, and their blood glucose levels were recorded. Colorimetric measurement of blood glucose was performed using the NO GL 13 20 kit, which was obtained from Biodiagnostic Co. in Giza, Egypt. The color turned reddish violet and was detected at 553 nm **[12].**

Malondialdehyde level (MDA level) and Total antioxidant capacity (TAC) were assessed in brain tissue, and (Biodiagnostic, Giza, Egypt) was the source of all the reagents. The thiobarbituric acid (TBA) method was used to assess the MDA levels in brain structures, and the pink chromogen was detected at 532 nm. [13]. TAC level is determined by combining a specific quantity of exogenously provided hydrogen peroxide (H2O2) with

antioxidants present in the sample. Colorimetry is used to determine the residual H2O2. [14]. the Biochemistry department at Zagazig University's College of Medicine does all biochemical measurements.

Histological Study:

I. **Light microscopic technique [15].**

Before being processed and embedded in paraffin to create five-um thick paraffin slices, the specimens were fixed in 10% formal saline for 48 hours. They were then dyed with

A- Hematoxylin and eosin (H&E) stains for histological analysis [15].

B- Congo red stain for amyloid deposits demonstration [16]. A section of the block with a thickness of 5-10 µm was cut. Dewax for five minutes in Xylene. They were hydrated with distilled water at the conclusion and progressively increasing alcohol concentrations (100%, 90%, and 70%). Spend 15 to 20 minutes staining in Congo red solution. Use distilled water to rinse. Differentiate rapidly in an alkaline alcohol solution (5–10 dips). Rinse for one minute under the tap. Use Gill's hematoxylin as counterstain for thirty seconds. Give it a two-minute rinse under the tap. After being cleaned and dehydrated, they were mounted in Canada balsam.

C- Immunohistochemical staining: [17] for labeling and identification of:

- **Glial Fibrillary Acidic Protein (GFAP):** for astrocytes **[18]**.
- **Synaptophysin (SYP):** a marker for synaptic density and integrity **[19]**.

Using the initial antibodies listed below, A 1:100 concentration of monoclonal mouse anti-glial fibrillary acidic protein (anti-GFAP) was utilized; it was supplied by Sigma Laboratories (CAT. #MA5-12023). The avidine biotin peroxidase system used in the Universal kit was made in the UK by Novacastra Laboratories Ltd. Mouse monoclonal antibody against synaptophysin (CAT #:A0010) supplied by Lab Vision Laboratories. The avidin biotin peroxidase system was used to perform immunohistochemical responses. The pancreas for synaptophysin and the brain for GFAP served as positive controls. Sections of negative control were run. For every specimen, a substitute primary antibody was added and stained with Mayer's hematoxylin.

GFAP: The astrocytes' dark cytoplasm and cell membrane served as indicators of the favorable outcomes. This strain is thought to be specific for the fibrillary acidic protein intermediate filaments present in astrocytes; nerve cells and even other glial cell types like oligodendrocytes or microglial cells do not have it [**20]. SYP:** The surface of the neuronal cell bodies showed brown staining, which suggested positive results. **[21].**

Leica DM500 microscope was used to view the images, and digital cameras were used to capture the photos and add a scale bar to the photomicrographs.

Transmission electron microscope (TEM) technique [22]:

Each animal's cerebral hemispheres were placed on a dental wax sheet with a drop of gluteraldehyde (2.5%) in cacodylate buffer (0.1M) for hippocampus extraction. The hippocampal samples were then sliced into tiny pieces using a sharp scalpel **[23]** and were fixed at pH 7.4 and 4ºC in 2.5% glutaraldehyde. After that, the specimens were prepared for electron microscopic analysis. The ultramicrotome was used to cut ultrathin (80 nm) sections. Double staining technique**:** Ultrathin sections were stained with uranyl acetate and lead citrate **[24].** An electron microscope (JEOL JEM100CX, Jeol Ltd, Tokyo, Japan) was used to analyze and photograph the ultrathin sections at Zagazig University's Microscope Unit and Ain-Shams University's Electron Microscope Unit.

II. Image Analysis and Morphometric Studies:

The following parameters were measured using morphometric analysis on serial sections stained with H&E, anti-GFAP, and anti-SYP immunohistochemical reactions: thickness of the pyramidal cell layer of the CA1 area (PCL), thickness of the granule cell layer of the DG (GCL), the percentage area of GFAP immunoreactions in CA1 and DG, and optical density of SYP immunoreactions in CA1 and DG.

The Leica Qwin 500 image analyzer computer system (Leica Ltd., Cambridge, UK) was utilized in the Pathology Department's Image Analyzing Unit at Cairo University's Faculty of Dentistry to obtain data.

STATISTICAL ANALYSIS

The information was gathered, tallied, and presented as the average and standard error (means ± SE). A one-way statistical comparison was performed between the groups. The SPSS 20 Evaluation Version computer program (SPSS Inc., Chicago, IL) and post-hoc (least significant difference, or "LSD") tests were used after an

analysis of variance (ANOVA). At P<0.05, statistical significance was determined.

RESULTS

By the end of the experiment, compared to the normal rats (control groups), the rats in the Alzheimer's disease-induced by AlCl3 groups displayed mild weakness, carelessness with food intake, reduction in weight and feed consumption, as well as slowdown and decrease in exploratory behavior with regard to the modified T-maze test. This study's mortality rate was noted, with two fatalities in the curative group and three in the AD-induced group **(Table 1s)**.

Estimation of the mortality rate of adult male albino rats in the different studied groups.

Data collected from all control subgroups (Ia, Ib, and Ic); T-maze score, brain tissue MDA level and TAC level, statistical analysis as regard the mean value *Mean* ± *SE* (standard error) results that there was non-significant difference between different control subgroups **(Table 2s).** Therefore, the biochemical, morphometrical and histological results of subgroup Ia only are reported.

T-maze score:

When comparing the mean T-maze score of the several groups under study, the AD-induced group has the lowest score, followed by the therapeutic group, and the control group has the greatest score. The ameliorative group did not differ significantly from the control group. T-maze decreased in the curative group statistically significantly more than in the control and ameliorative groups (p~^0.05) **(Table 3s).**

MDA (nmol/gm tissue):

The control group had the lowest mean MDA value, while the AD-induced group had the highest mean MDA value, followed by the therapeutic group. The ameliorative group did not differ significantly from the control group. A statistically significant rise in MDA was also observed in the curative group when compared to the control and ameliorative groups **(Table3s).**

TAC (U/gm tissue):

The group with AD induced lower mean TAC values than the group with therapeutic values; however, this difference was not statistically significant (p>0.05). When compared to the other groups, the control group had the highest TAC value. The ameliorative group did not differ significantly from the control group. A statistically significant drop in TAC was also observed in the curative group as compared to the control and ameliorative groups **(Table).**

Blood glucose level (mg/dl):

There was no distinct difference in the mean blood glucose value across the various study groups **(Table3s).**

***Morphometrical results* (Table 4s;5s;6s)**

The thickness of the pyramidal cell layer (PCL) of CA1 and granular cell layer thickness (GCL) of DG in the different studied groups and the optical density of SYP (Table 4s;5s): there was a statistically significant decrease in the thickness of (PCL) and (GCL) of the AD- induced group and curative group compared to the control group While, there was statistically significant increase in curative group compared to AD-induced group. There was no statistically significant difference in the ameliorative group compared to the control group. On the other hand, there was a statistically significant decrease in the curative group compared to the ameliorative group.

The area percentage of GFAP in the field in the different studied groups in both CA1 area and DG (table): There was a high statistically significant increase (P < 0.05) observed in the AD-Induced group in comparison with both the control and ameliorative groups. There was no statistically significant difference in the ameliorative group compared to the control group. The ameliorative group revealed a highly significant decrease in area % in comparison to the AD-induced and curative group, although a significant statistical difference was represented Between AD- the AD-induced group and the curative group.

Histological results:

The results of the light microscopy examination of all control groupings (a-c) were very similar. As a result, only the control subgroup Ia's histology findings are presented.

1. ***H&E results: (plate I, II)***

H&E stained sections were employed for examination of the histological structure of the neuropil H&E stained Para sagittal sections of the hippocampus of the control adult male albino rats revealed that the hippocampus was C-shaped, projecting into the floor of the lateral ventricle. The hippocampus proper (Cornu Ammonis) with its four areas, CA1, CA2, CA3, and CA4, were seen. CA1 related to hippocampal sulcus (HS) which appeared as a deep groove. CA2/CA3 related to lateral ventricle, CA4 at hilus of dentate gyrus. The dentate gyrus (DG) has upper and lower blades and a crest (Figures 1a, 1b, 1c, **and 1d).** The hippocampal sulcus was difficult to

observe. Choroid plexus and lateral ventricle were seen **(Figure 1d).**

Higher magnification of boxed area A of Figure (1a) of the control group showed a part of Cornu Ammonis of the hippocampus CA1 area, which was formed of three layers: molecular, pyramidal, and polymorphic. The pyramidal nerve cell layer in the CA1 region was thick and composed of closely packed pyramidal cells with vesicular nuclei, prominent nucleoli, and pale basophilic cytoplasm. Neuroglial cells with darkly stained nuclei and normal pericellular hallo are noticed (Figure 2a). At a higher magnification of the boxed area, A of Figure (1b), the AD-induced group showed a part of Cornu Ammonis of the hippocampus area, which was formed of three layers: molecular, pyramidal, and polymorphic. The pyramidal layer contained large cells with shrunken, darkly stained nuclei and vacuolated cytoplasm. Multiple large glial cells with darkly stained nuclei were surrounded by wide, lightly stained spaces. A dilated blood vessel was seen (Figure 2b). At higher magnification of boxed area A of Figure (1c), the ameliorative group showed a part of Cornu Ammonis of the hippocampus area, which revealed closely packed pyramidal cells. Few pyramidal cells had pyknotic densely stained nuclei, while many of them appeared rounded with vesicular nuclei. Multiple neuroglial cells with dark stained nuclei surrounded by peri cellular spaces were seen. Blood vessels were detected as apparent normal compared to the AD-induced group (Figure.2c). A higher magnification of the boxed area A of (Figure. 1d) of the curative group showed a part of Cornu Ammonis CA1 area with its three layers: molecular, pyramidal and polymorphic. The CA1 area revealed a notable disruption arrangement of the pyramidal layer. Pyramidal cells separated from each other by glial cells, which appeared as dark nuclei surrounded by pericellular space. Multiple pyramidal cells appeared lightly stained nuclei with prominent nucleoli, and few of them were still shrunken with pyknotic basophilic nuclei. Blood vessels were seen **(Figure 2d). A higher magnification of boxed area B of** Figure (1a) of the control group showed the dentate gyrus (DG) of the hippocampus that consisted of a molecular layer, granular cell layer, and polymorphic cell layer. The granular cell layer contained many compactly arranged mature granule cells with rounded pale vesicular nuclei. Multiple small neurons with oval dark nuclei were detected in the subgranular zone (SGZ) (Figure **4a).**

A higher magnification of **boxed area B of figure (1b)** of AD-induced group, showed dentate gyrus with granular cell layer which contained shrunken granule cells with multiple pyknotic dark stained nuclei. Multiple immature neurons with oval dark nuclei were seen in the subgranular zone (SGZ). The (SGZ) appeared vacuolated. Numerous large glial cells with darkly stained nuclei surrounded by lightly stained wide spaces were also seen in molecular and polymorphic layers. Dilated and congested blood vessels were detected **(Figure.4b).**

At higher magnification of **boxed area B of figure (1c)** of ameliorative group, showed the dentate gyrus (DG) of the hippocampus. The granular cell layer contained a few granule cells with shrunken, darkly basophilic pyknotic nuclei, while most of them appeared rounded with pale vesicular nuclei. Numerous immature neurons with oval dark nuclei were detected in the subgranular zone (SGZ). Multiple glial cells with darkly stained nuclei surrounded by lightly stained spaces were also seen. The blood vessel was also seen near normal (Figure.4c). A higher magnification of the boxed area B of (Fig.1d) of the curative group showed dentate gyrus, which consisted of regular organization of molecular layer, granular cell layer, and the polymorphic layer with the subgranular zone (SGZ). The granular cell layer (GC) contained compactly arranged mature granule cells with rounded pale vesicular nuclei and pale basophilic cytoplasm, and some of them still pyknotic with darkly stained nuclei. An apparent few immature neurons with oval dark nuclei were detected in the subgranular zone (SGZ). Numerous glial cells with darkly stained nuclei surrounded by lightly stained spaces were also seen **(Figure 4d).**

Congo red stained sections were applied for amyloid plaque demonstration:

Congo red stained para sagittal sections of the control group revealed that the CA1 area of Cornu Ammonis had no red color for amyloid plaque deposits staining in molecular or pyramidal or polymorphic layer **(Figure. 3a).** CA1 area with a pale red deposit in pyramidal cell layer and red color in a deformed blood vessel with cellular infiltration were also observed **(Figure. 3b).** CA1area revealed no red color deposits within their three layers and nor in blood vessels **(Figure. 3c).** CA1 area revealed extracellular red amyloid deposits in pyramidal layer. A dilated blood vessel was seen **(Figure 3d).** Congo red-stained para sagittal sections of the control group revealed that

dentate gyrus was free from any red deposits of amyloid plaque **(Figure. 5a)**

In AD-induced group, DG of the hippocampus with intense dense red color deposits within the 3 layers; molecular, granular and polymorphic layer (**Figure. 5b)** DG appeared clear from any red coloration of amyloid deposits **(Figure.5c).** Congo red stained para sagittal sections of curative group revealed obvious red deposits in the polymorphic layer **(Figure.5d).**

Immunuhistochemical results (plates III,VIs):

Immunohistochemically stained sections for GFAP were prepared to study astrocyte size and number: Immunohistochemically stained sections for GFAP of the control group revealed that area CA1 of Cornu Ammonis and DG appeared with positive immune reaction in the cytoplasm of astrocyte and their processes in the form of dark brown coloration. Few of astrocytes were seen dispersed **(figure.6a; 8a).** CA1of Cornu Ammonis and DG of AD-induced group appeared with strong positive immune reaction in the cytoplasm and processes of astrocytes in the form of dark brown coloration. Astrocytes appeared larger in size with thick processes dispersed **(Figure 6b; 8b).** In Ameliorative group, CA1 area and DG appeared with a mild positive immune reaction in cytoplasm of astrocytes and their processes. Many astrocytes were dispersed among their layers **(figure.6c; 8c).** Immunohistochemical stained sections of hippocampus of curative group for **GFAP** revealed area CA1and DG with moderate positive immune reaction of GFAP in the cytoplasm of astrocytes and their processes in form of brown coloration. They appeared large in size, with multiple thick processes dispersed in between their layers (Figure **6d; 8d)**.

Immunohistochemically stained sections for SYP were achieved as an indicator of synaptic density: Immunohistochemically stained sections for SYP of the control group revealed that area CA1 of cornu Ammonis appeared with the positive immune reaction of SYP on the surface of the pyramidal cell bodies with their apical dendrites and DG with the positive reaction of presynaptic terminals at surfaces of granule cells in the granule cell layer in the form of brown coarse beaded granules **(figure.7a; 9a)** In AD-induced group, CA1 area appeared with marked decrease in the immunoreactivity of SYP on the surface of the pyramidal cell bodies with their apical dendrites in the pyramidal layer, and DG revealed with a marked decrease in the immunoreactivity of SYP on the surface of the granular cells in from of faint brown coloration between granular cells **(figure.7b; 9b).** In the Ameliorative group, the CA1 area and DG appeared with a strong positive immune reaction of SYP on the surface of pyramidal cells with their apical dendrites and granular cells in the form of brown coloration. Some of them still showed a decrease in immunoreactions (Figure **7c; 9c).** Immunohistochemically stained sections of the hippocampus of the curative group for SYP of area CA1and DG showed a mild increase in immunoreactivity on the surface of the pyramidal cell bodies with their apical dendrites and on the surface of the granular cell, while other cells revealed diminution immunoreactions **(figure.7d; 9d)**

Transmission Electron Microscope: (Plate. Vs; VIs; VIIs)

Ultrathin sections were applied for TEM examination to illustrate the ultrastructure of the hippocampus (Plate. V): Examination of ultrathin sections from part of the hippocampus of **The control group showed pyramidal cells with a well-demarcated oval euchromatic nucleus and prominent nucleolus** surrounded by a regular nuclear membrane. The cytoplasm contained normal rod shaped mitochondria and others spherical were seen. Narrowing cisternae of rough endoplasmic reticulum (rER) was presented as parallel tubules near the nucleus, and free ribosomes and neurofilaments were observed **(Figure. 10a).** TEM of pyramidal cells of the same group revealed oval euchromatic nucleus surrounded by an electron-lucent cytoplasm contained multiple numerous mitochondria with prominent cristae and microtubules as shown in **(Figure.11a).** TEM revealed oligodendroglia cells with an oval euchromatic nucleus. The surrounding neuropil exhibited multiple nerve fibers surrounded by intact regular myelin sheaths **(Figure 12a). TEM revealed the ultrastructure of the neurovascular unit (capillary), which consists of endothelial cells with a flat euchromatic nucleus lining the capillary lumen, which contains** a red blood corpuscle (RBC). Electron dense tight junction was observed **(Figure.13a).**

Plate . (VI): Examination of ultrathin sections from part of hippocampus of **The AD-induced group** showed two adjacent pyramidal cells. One of them had a shrunken nucleus with chromatin condensation. Another pyramidal cell had a rounded heterochromatic nucleus. Numerous vacuoles were dispersed in the

disorganized neuropil. Mitochondria with disturbed cristae were observed **(Figure 14b).TEM showed that oligodendroglia appeared to have a heterochromatic nucleus and an** irregular nuclear membrane. The surrounding dense cytoplasm contained (rER) and an elongated dense vacuole. Multiple nerve axons with irregular distorted myelin sheath folding and vacuolated axoplasm were seen **(Figure.15b)**. Microglial cells appeared with elongated heterochromatic nuclei with peripheral chromatin condensation, the surrounding cytoplasm contained electron-dense residual bodies and mitochondria **(Figure.16b)**. The neurovascular unit (NVU) of **AD-induced group** consisted of multiple endothelial cells lining capillary lumen which contained multiple (RBC), resting on apparently interrupted thick basement membrane (BM) **(Figure.17b)**.

Plate. (VII): Examination of ultrathin sections from part of hippocampus of EMP –treated groups (ameliorative and curative). **The ameliorative group showed multiple neurons preserved at the utmost of their normal appearance, which revealed pyramidal cells with euchromatic well, demarcated oval nuclei,** and prominent nucleoli. The electron-lucent cytoplasm contained (rER) and free ribosomes (**Figure 18c).** Oligodendroglia cells appeared with irregular indented euchromatic nucleus. Nerve axons with intact regular myelin and others with irregular myelin sheath were observed (**Figure.19c).** Astrogliosis appeared in this group in form of aggregates of adjacent neuroglial cells; elongated nucleus of microglia, electron dense indented nucleus of astrocyte and another cell with electron lucent indented nucleus mostly different stages of astrocytes (**Figure.20c**).In ameliorative group, the NVU consisted of endothelial cells with electron dense tight junction between them. Intact BM was observed within NVU and capillary lumen contained multiple (RBCs). Astrocyte end feet appeared as a thin clear zone bordered on BM (**Figure.21c**).

Curative group: Two adjacent pyramidal cells with oval euchromatic nuclei and prominent nucleoli surrounded by irregular nuclear membrane. Nuclear cleft of hippocampal neuron (nuclear envelope invagination) was observed. The surrounding electron-lucent cytoplasm contained mitochondria and dilated rER **(Figure.22d).** Another pyramidal cell of the curative group still displayed irregular and swollen of nuclear membrane which invaginated inside the nucleus forming nuclear reticulum .swollen mitochondria were observed (**Figure.23d).** An oligodendroglia cell appeared with irregular euchromatic nucleus. Thick intact myelin coats of multiple nerve fibers were seen **(Figure24d).** In curative group, TEM showed NVU consisted of heterochromatic endothelial cells with electron dense tight junction lining capillary lumen. Astrocyte cell with heterochromatic nucleus was adjacent to the capillary unit. Swollen astrocyte end feet appeared as a wide clear zone bordered on BM. Regular myelinated nerve axons were close to capillary unit was observed while others were with disturbed myelin coat **(Figure.25d).**

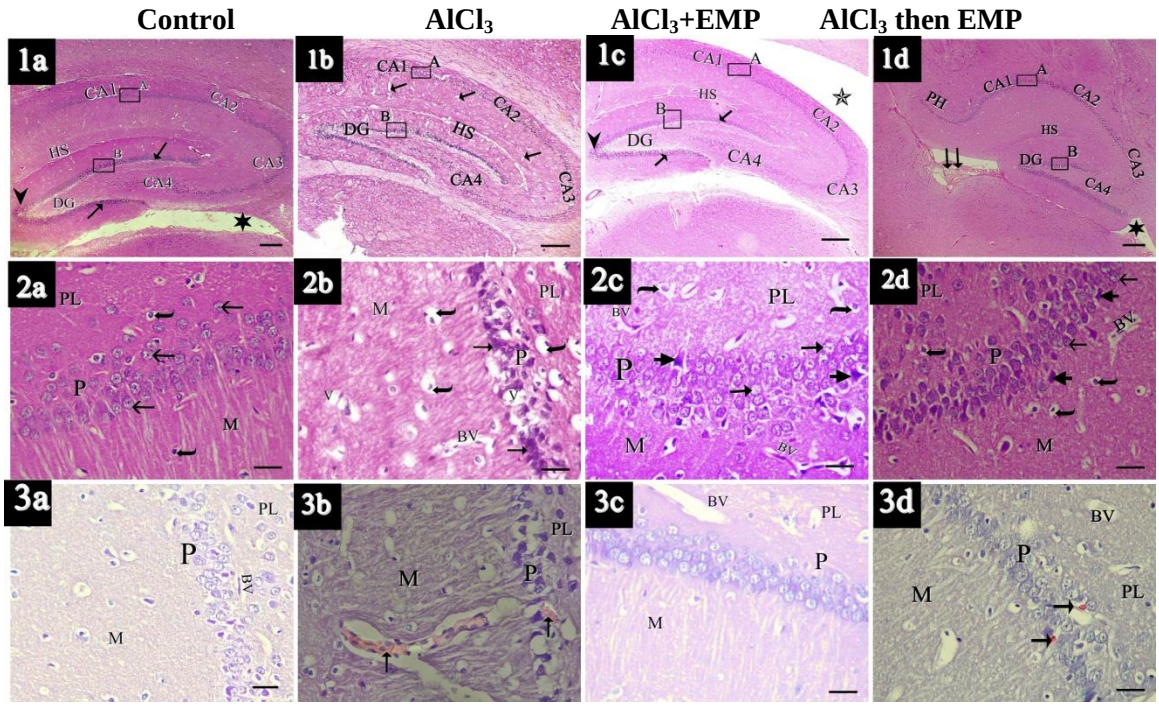

Plate. I: Figure (1): A photomicrograph of a para sagittal sections in the hippocampus stained by H&E showing normal panoramic view of hippocampus presented as hippocampus proper (Cornu Ammonis) and dentate gyrus (DG). Cornu Ammonis regions CA1, CA2, CA3 and CA4 can be seen.CA1 related to hippocampal sulcus (HS) which appears as a deep groove, CA2/CA3 related to lateral ventricle (star).CA4 is seen at hilus of dentate gyrus. DG has upper, lower blades (arrows) and crest (arrow head). **(a) Control group** reveals normal panoramic view of the hippocampus as previous mentioned. **(b) AD- induced group** shows (DG) with its toothed surface can be seen. Multiple diffuse vacuoles are observed (arrows). **(c) Ameliorative group** reveals normal hippocampus layout regions. **(d) Curative group** displays hippocampal sulcus (HS) is difficulty observed adjacent to the CA1 area .choroid plexus (double arrow) and lateral ventricle (star) are seen. **(H&E, X40, scale bar200µm).**

Figure (2): A higher magnification of the **boxed area A of (Figure.1)** in the inset showing a part of Cornu Ammonis CA1 area with its three layers: molecular (M), pyramidal (P) and polymorphic (PL). **(a) Control group** showing thick Pyramidal layer (P) composed of closely packed pyramidal cells with large vesicular nuclei with prominent nucleoli and pale basophilic cytoplasm (arrows). Neuroglial cells with dark stained nuclei and normal pericellular hallo are noticed (curved arrows). **(b) AD- induced group** displays Pyramidal layer which contains large cells with shrunken darkly stained nuclei (arrows) and vacuolated cytoplasm (V). Multiple large glial cells with darkly stained nuclei are surrounded by wide pericellular wide spaces are seen (curved arrows). Dilated blood vessel is seen (BV). **(c) Ameliorative group** reveals CA1 area with closely packed pyramidal cells, multiple of them appear with lightly stained nuclei and prominent nucleoli (arrows).While others are still shrunken with darkly stained basophilic pyknotic nuclei (thick arrows). Numerous glial cells with dark stained with pericellular space are also seen (curved arrow).Blood vessels (BV) are observed near to normal. **(d) Curative group** showing The CA1 area reveals a notable disruption arrangement of the pyramidal layer; pyramidal neural cells become separated from each other by glial cells (curved arrows) which appear with dark nuclei surrounding by pericellular space. Multiple pyramidal cells contain lightly stained nuclei with prominent nucleoli (arrows) while few of them are still shrunken with pyknotic nuclei (thick arrows).Blood vessels (BV) are seen. **(H&E, X400, scale bar20µm).**

Figure (3): A photomicrograph of Para sagittal sections in the hippocampus stained by Congo red stain for amyloid plaque demonstration. (a**) Control group** showing No red coloration for amyloid plaque deposits staining in molecular (M), pyramidal (P) or polymorphic (PL) layers. (**b) AD- induced group** reveals a pale red color in pyramidal cells layer and also a red deposit in deformed blood vessels are detected (arrows). **(c) Ameliorative group** reveals no red color deposits within the three layers of CA1 and nor in blood vessels. **(d) Curative group** showing CA1 area with extra cellular red amyloid deposits (arrows) in pyramidal (P) layer. Dilated blood vessels (BV) are seen. **(Congo red, X400, scale bar20µm).**

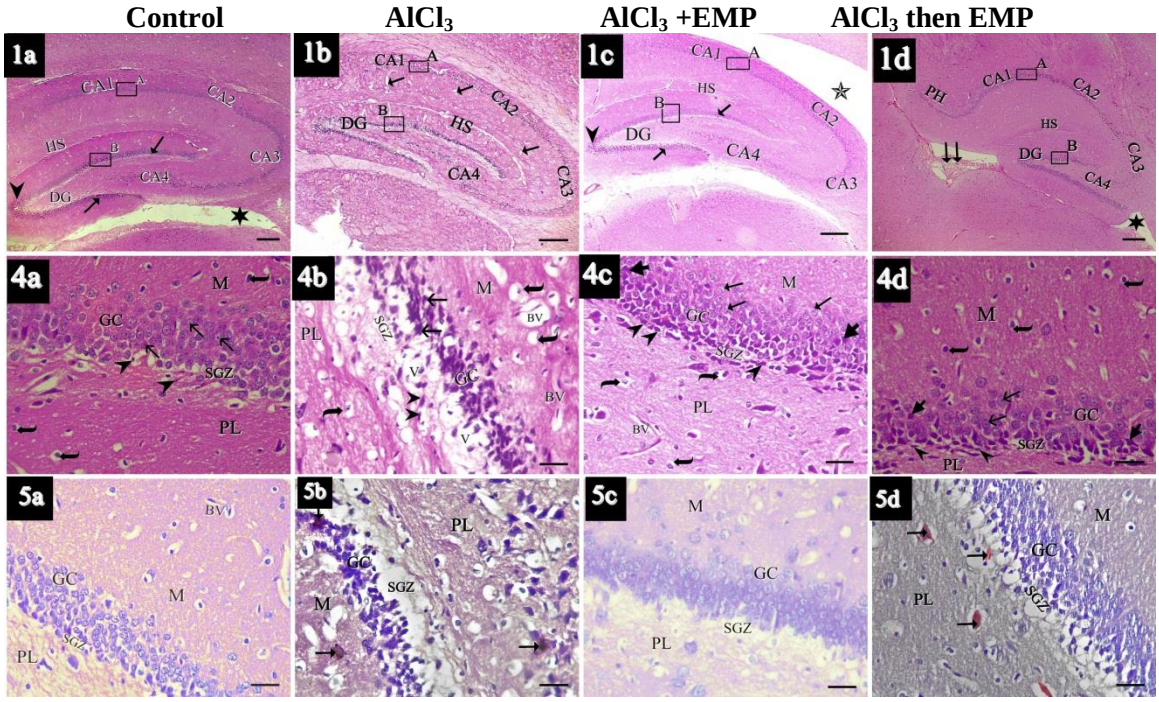

Plate. II: Figure (1): A photomicrograph of a para sagittal sections in the hippocampus stained by H&E showing normal panoramic view of hippocampus presented as showing hippocampus proper (Cornu Ammonis) and dentate gyrus (DG). Cornu Ammonis regions CA1, CA2, CA3 and CA4 can be seen.CA1 related to hippocampal sulcus (HS) which appears as a deep groove, CA2/CA3 related to lateral ventricle (star).CA4 is seen at hilus of dentate gyrus. DG has upper, lower blades (arrows) and crest (arrow head). . **(H&E, X40, scale bar200µm).**

Figure (4): A higher magnification of the **boxed area B of (Figure.1)** in the inset showing DG of the hippocampus consists of molecular layer (M), granule cell layer (GC) and polymorphic cell layer (PL). **(a) Control group** shows granule cell layer (GC) of dentate gyrus that contains closely packed mature granule cells with rounded pale vesicular nuclei (arrows). Multiple small neurons with oval dark nuclei (arrow heads) in the subgranular zone (SGZ) are seen. Neuroglial cells with dark stained nuclei and normal pericellular hallo are noticed (curved arrows). Normal blood vessels (BV) with normal perivascular space are observed. **(b) AD-induced group** showing DG with granular cell layer (GC) which contains shrunken granule cells with multiple pyknotic dark stained nuclei (arrows). Multiple immature neurons with oval dark nuclei (arrow heads) are seen in the subgranular zone (SGZ). (SGZ) appears vacuolated (V). Numerous large glial cells with darkly stained nuclei surrounded by lightly stained wide spaces (curved arrows) are also seen in molecular (M) and polymorphic (PL) layers. Dilated and congested blood vessels (BV) are detected. **(c) Ameliorative group** reveals granule cell layer (GC) containing multiple mature granule cells with rounded pale vesicular nuclei (arrows) while few granule cells are still shrunken with dense basophilic pyknotic nuclei (thick arrows).Numerous immature neurons with oval dark nuclei (arrow heads) are seen in the subgranular zone (SGZ). Multiple glial cells with darkly stained and lightly stained nuclei surrounded by pericellular space are detected (curved arrows). Blood vessel is also seen (BV) near to normal. **(d) Curative group** showing DG consists of regular organization of molecular (M), granule cell (GC) and the polymorphic (PL) layers. The granule cell layer (GC) contains compactly arranged mature granule cells with rounded pale vesicular nuclei (arrows) and pale basophilic cytoplasm, and some of them still pyknotic with darkly stained nuclei (thick arrows). Apparent few immature neurons with oval dark nuclei are detected in (SGZ) (arrow heads). Numerous glial cells with darkly stained surrounded by pericellular space are also observed (curved arrows). **(H&E, X400, scale bar20µm).**

Figure (5): A photomicrograph of Para sagittal sections in the hippocampus stained by Congo red stain for amyloid plaque demonstration. (a**) Control group** showing DG with free from any red coloration for deposits of amyloid plaques within molecular (M), granular cell (GC) and polymorphic (PL) layers. **(b) AD- induced group**

showing DG with intense dense red color deposits within the 3 layers; molecular, granular and polymorphic layer. **(c) Ameliorative group** showing The DG appears clear from any red color of amyloid deposits. **(d) Curative group shows** DG with evident red focal deposits (arrows) appear in polymorphic (PL) layer **(congo red, X400, scale bar20µm**).

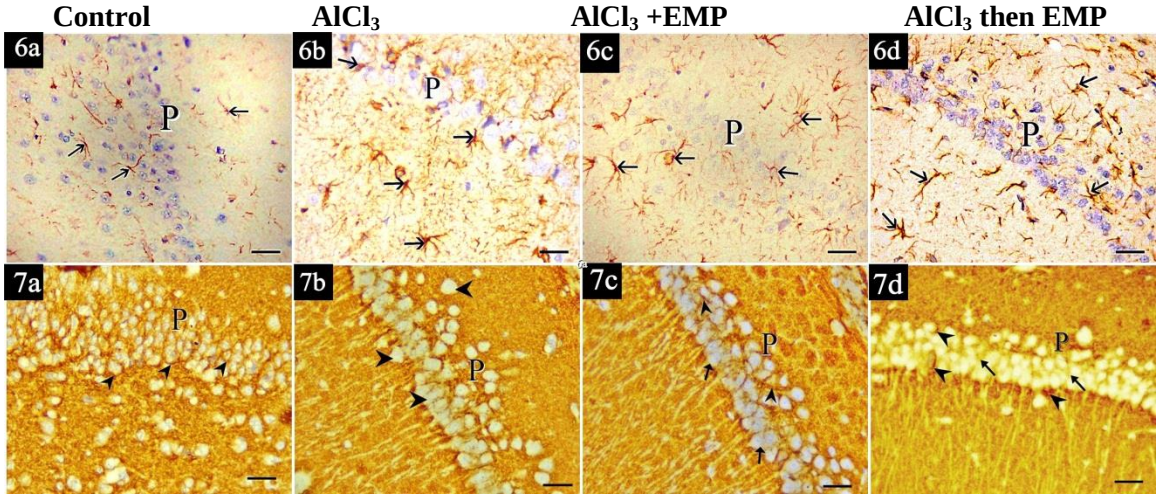

Plate. III: Figure (6): photomicrograph of an immunohistochemical stained section in CA1 of the hippocampus for GFAP. Positive immune reaction of GFAP is in the cytoplasm of astrocyte and their processes in the form of brown coloration (arrows). Astrocytes are dispersed in between pyramidal cell (P) layer. **(a) The control group** showing positive immune reaction of GFAP and Few astrocytes are in between pyramidal cell (P) layer. **(b) AD-induced group** showing strong positive immune reaction for GFAP. Astrocytes appear larger in size with thick processes. Many astrocytes dispersed the layers of CA1. **(c) Ameliorative group** showing mild positive immune reaction of GFAP. **(d) Curative group** showing moderate positive immune reaction of GFAP. Astrocytes appear large in size with multiple thick processes dispersed in between the pyramidal cell (p) layer. Many astrocytes are seen dispersed among layers of CA1. **(Immunoperoxidase reaction for GFAP, X400, scale bar20µm).**

Figure (7): photomicrograph of an immunohistochemical stained section in CA1 of the hippocampus for SYP. Positive reaction of SYP at the surface of Pyramidal cell bodies (P) and their apical dendrites in the pyramidal cell layer in form of brown coarse beaded granules (arrow heads). **(a) Control group** shows strong positive reaction of SYP. **(b) AD- induced group** exhibits marked decrease in the immunoreactivity of SYP in form of faint brown coloration (arrow heads). **(c) Ameliorative group** showing marked increase in number of pyramidal cells with immunoreactivity of SYP on the surface of the their cell bodies (P) and their apical dendrites in the pyramidal layer(arrow heads) while others show still decrease in immunoreactions (arrows). **(d) Curative group** reveals mild increase in immunoreactivity on the surface of the pyramidal cell bodies (P) with their apical dendrites in the pyramidal layer (arrow heads) while other cells still exhibit decrease in immunreactions (arrows).

DISCUSSION:

We used the popular Modified T maze test in this study to assess how AlCl3 affected the rats' memory and capacity to learn. The current study's findings showed that taking AlCl3 orally for eight weeks caused a progressive decline in spatial memory as measured by this test; in particular, we observed that AD-group II's T maze score significantly decreased in comparison to the other groups. In AD mice, Davis et al.'s [25] T maze score significantly decreased. The neurobehavioral abnormalities and memory impairment linked to AD may potentially be explained by this disturbance.

In the present study, statistical analysis of the mean values of malondialdehyde **(MDA)** in the brain tissue, showed statistically highly significant increase in the AD-induced group II relative to the other cohorts. A rat model of Alzheimer's disease created by AlCl3 showed similar results [26]. Lipid peroxidation produces MDA, which was once thought to be a biomarker for oxidative stress. MDA has been demonstrated to alter the cellular membrane's structure, which may lead to alterations in the DNA within the cell **[27]**.

Skalny et al. [28] said that the neurotoxic effects of Al exposure also contributed to the elevated MDA level. Its common toxic characteristics, which include prooxidant, proinflammatory, and proapoptotic activity in a range of cell lines and tissues, mediate this effect. Because of its high glucose and oxygen consumption, low mitotic rate, low level of antioxidant enzymes, and highly unsaturated lipid composition, brain tissue is particularly susceptible to damage from free radicals **[29]**.

The present study's statistical analysis of the total anti-oxidant capacity (TAC) mean values revealed a significantly lower level of TAC in the Alzheimer-induced group II as compared to the other groups. This is consistent with Chen et al.'s [26] observation of a significant decrease in TAC levels in an Alzheimer's rat model produced by AlCl3.

Regular exposure to AlCl3 raised the levels of MDA in different brain regions while markedly lowering the status of TAC and the antioxidant enzyme super oxide dismutase (SOD).Oxidative stress assisted neurotoxicity is the main pathogenic event in AD neurodegeneration. Endogenous antioxidants are produced by living cells and serve as a buffer against accumulated free radicals as well as protection against oxidative damage. The amount of free radicals that have collected is greater than what cells can neutralize **[30].**

Examining parasagittal slices of adult male albino rats' hippocampal tissue from AD-induced group II showed several diffuse vacuoles when stained with hematoxylin and eosin (H&E) at panoramic view. Sections of the hippocampal proper's CA1 stained with (H&E) showed evidence of degeneration in the form of reduced and distorted pyramidal cells with vacuolated cytoplasm and darkly stained pyknotic nuclei. Additionally, DG displayed a granular cell layer that was distorted and shrunken, with vacuolated cytoplasm. These indications of cellular deterioration and death were detailed by **Lakshmi et al. [31] and Gazia, [32]** who reported same results.

As well, these findings were validated by TEM analysis, which showed shrinking pyramidal cells with heterochromatic nuclei. In addition to diffusely damaged myelination of various nerve axons, mitochondria were swollen with distorted cristae and numerous vacuolation scattered inside the malformed neuropil. Comparable outcomes were reported by **Gao et al. [33]** who detailed these alternations brought about by hippocampus damage in an Alzheimer's rat model.

These findings could be explained by **Kumar et al. [34]** Researchers found that Al, a strong pro-oxidant, enhanced lipid peroxides in the cortex and hippocampus, and caused oxidative stress that resulted in structural damage to neuronal mitochondria in the hippocampal neurons. It also targets mitochondria, which results in the activation of proapoptotic proteins like caspase-3 and the release of cytochrome c. In the end, this causes apoptosis in neurons. Numerous investigations revealed that exposing mammalian cells to Al increases cell death in a time- and dose-dependent way, exhibiting hallmarks of apoptosis include chromatin that is hypercondensed and asymmetrically structured and shrinking cell bodies **[35].**

Examining H&E-stained sections from the hippocampal regions of adult male albino rats, the current study found that some neuroglial cells had nuclei that were strongly stained and surrounded by lightly stained space. Furthermore, TEM revealed irregular heterochromatic nuclei in neuroglial cells. These results have contributed to the process of reactive gliosis, a highly typical non-specific response to nearly any type of CNS injury. The astrocytes' hypertrophy and proliferation are the cause of this reaction [**36].** DG examination revealed distorted granular cells and oval nuclei of developing neurons. In the dentate gyrus, there was a noticeable decrease in mature granular cells (GC) and a large number of immature neurons in the subgranular zone (SGZ). **Li et al. [37] and Arredondo et al. [38]** explained these findings by stating that free-radical oxidative stress caused by Al damages neural membranes in the brain, which leads to oxidative damage-associated neuronal cell death and the immature formation of neurons in the dentate gyrus in AD. The present morphometric evaluation of the GC thickness and pyramidal layer in the **AD-induced group II** revealed a very low thickness as compared to the control, which validated the microscopic findings.

This investigation also revealed the presence of extracellular amyloid plaques in CA1 and DG sections stained with Congo red. **Cioanca et al. [39] & Jadhav and Kulkarni, [29]** reported outcomes that were comparable. The semicrystallized β-sheet protein is turned a vivid salmon orange color by the Congo red stain, which is used to diagnose amyloidosis. This is because

Congo red has a strong affinity for amyloid deposits **[40].**

These findings could be explained by **Singh et al. [9]** who documented the neurotoxicity produced by an excess of aluminum chloride in rats. It causes cytoskeleton protein misfolding, which results in the development of tau neurofibrillary tangles and amyloid beta plaques. **Ricchelli et al. [41] and Zaky et al. [42]** said that Al promotes the synthesis and aggregation of extracellular Aβ.

The association between Al and Aβ was confirmed by **Exley, [43]** who stated that Al and Aβ42 could form a complex. It promotes β-sheet precipitation and makes it easier for Aβ to penetrate the BBB.

Bhattacharjee, [44] explained that Triggering receptor expressed by myeloid cells 2 (TREM2). TREM2 acts as a cell microglia's surface receptor. The transmembrane sensor–receptor glycoprotein is essential for the central nervous system to phagocytose Aβ42 peptides. It may be able to recognize and detect molecular tags on Aβ42 peptides because it can massage molecular sensors into the extracellular area. In addition, aluminum sulfate has been shown to stimulate ROS-dependent miRNA-34a, a member of a small family of pro-inflammatory microRNAs. The up-regulated miRNA-34a suppresses the expression of TREM2 in the membrane of microglial cells, hence decreasing their ability to phagocytose Aβ42 peptide monomers. This leads to an eventual accumulation of Aβ42 peptides in the extracellular region. **[45].**

This study found that the distorted blood capillaries in the CA1 region had amyloid deposits inside of them. This was clarified by **Miyakawa [46] and Korte et al. [47**], who reported that there was a correlation between capillary blood vessels and the amyloid fibrils that produced the senile plaques, and that capillaries in the brains of AD patients displayed an aberrant focally-constricted shape. Oligomeric Aβ may trigger contractile pericytes, which in turn cause the constriction of capillaries. Cerebral hypoperfusion results from capillary constriction, which exacerbates neuronal deterioration and impairs cognition.

Examining immunohistochemically stained sections from AD-induced group II under a light microscope revealed a statistically significant increase in the mean value of the area percent of GFAP immunoreaction in AD-induced group II compared to the control group, as well as a remarkable increase in the positive immunoreaction for GFAP within the cell bodies and processes of astrocytes. The accepted method for evaluating astrocytic gliosis is GFAP. It is particularly prevalent in the cytoplasm of hypertrophy or reactive astrocytes **[36].** Comparable outcomes were noted by **Kamar et al. [48].**

TEM further demonstrated a large microglial cell and the electron-dense residual bodies in its cytoplasm. oligodentrocyte with an uneven nuclear membrane and heterochromatic nucleus; elongated dense vacuoles and rough endoplasmic reticulum (rER) were present in the surrounding cytoplasm. Vacuolated axoplasms and extended myelin sheath folding characterize many myelinated nerve axons with irregularly deformed sheath coats. Comparable outcomes were reported by **Desai et al. [49] and El Hajj et al. [50].**

The main characteristics of AD include synaptic loss, astrocytosis, neuronal degeneration, and microgliosis **[51].** According to **Cao et al. [52]**, microglia and astrocyte activation is the mechanism via which Al accumulation results in neuroinflammation. Proinflammatory cytokines are released by reactive astrocytes, which encourage the recruitment of monocytes and microglia to the damaged location and the surrounding Aβ plaques. Increased microglia proliferation is linked to amyloid deposition, but not reactive astrocytes.

Pathak and Sriram, [53] revealed that astrocytes, the type of neuroglia with the largest concentration in the brain, are essential to preserving the central nervous system's physiological function. Astrocytes are positioned in the center to protect the BBB, control cerebral blood flow, and control the neurovascular unit (NVU). Neurons, astrocytes, and endothelial cells make up the (NVU). The astrocytes' tiny processes penetrate the neuropil in the grey matter to make contact with the pia mater, ependymal cells, dendrites, synapses, and neuronal cell bodies. The dense network of fine glial processes, neuronal processes (axons and dendrites), and fibrils in the gray matter of the central nervous system that is not comprised of cell bodies is referred to as the neuropil by **Pannese [54].** More than 100,000 synapses and several neurons can connect with a single astrocyte **[55].**

Numerous investigations also stated that the pathophysiology of neurodegenerative illnesses is significantly influenced by the balance between the two categories. It is well recognized that the production of neurotrophic factors and phagocytosis of cellular debris by active microglia have neuroprotective effects. However, activated

microglia exacerbate neuronal damage by producing high levels of pro-inflammatory cytokines such TNF-alpha, IL-1β, and IL-6, as well as reactive oxygen species (ROS) and nitric oxide (NO) **[56].** Microglia has been described as having two faces: a beneficial one and a harmful one. Microglia activation is beneficial during the early stages of AD, but as the disease progresses, it becomes detrimental **[57].** Dilated ER cisternae were visible in this study's ultrathin hippocampal slices examined by TEM. According to **Kandimalla et al. [58]**, stress is induced in the endoplasmic reticulum (ER) of rabbit brain by both Al maltolate and Aβ42. The elongated dense vacuoles in the oligodentrocyte of the AD-induced group in this study may be elongated mitochondria or autophagosomes, as **Nahirney and Tremblay [59]** reported that dark oligodentrocyte revealed cellular stress markers such as dilated rER, elongated mitochondria, Golgi dilation, and autophagosomes.

The morphometric analysis corroborated the light microscopic observation of a notable reduction in Synaptophysin (SYP) immunoreactivity on the surface of pyramidal cells and their apical dendrites, as well as the surface of granule cell bodies with their apical dendrites, in the AD-induced group II. When comparing the mean value of the optical density of the (SYP) immunoreaction in AD-induced group II to the control group, statistical analysis revealed a substantial drop. **Lippa and Rosso [60]** found a similar result in Broca's region of the human cortex. In the current investigation, synaptic loss in the hippocampal region brought on by AD produced by Al administration was measured using SYP. These results were in line with **Taha et al.[61].**

A decrease in synaptophysin expression is indicative of synaptic impairments in many neurodegenerative disorders, as explained by **Honer [62].** According to **Shamasundar et al. [63]**, oxidative products like MDA, carbonyls, peroxynitrites, and enzymes like superoxide dismutase are released into neurons upon exposure to aluminum. This causes oxidative damage and induces disruption of the Golgi apparatus, as well as a decrease in synaptic vesicles and a reduction in axonal mitochondria turnover. **Walton, [64]** provided evidence in favor of the theory that long-term Al poisoning damages the cortex and hippocampi, altering both dendritic branches and axons.

TEM was used in this investigation to detect the NVU. The AD-induced group's NVU ultrastructurally revealed a disrupted unit that appeared to thicken interrupted BM. Additionally; the astrocyte end feet in the curative group were swollen. Otherwise, endothelial cells with electron-dense tight junctions were seen in ameliorative group IIIa. We observed contact astrocyte end foot surrounded by BM in a distinct zone. Similar results were observed by **Hayden [65],** who explained that insulin resistance and type 2 diabetes in a rat model led to NVU malfunction. Moreover, **Hayden et al. [66]** found that administering 10 mg of EMP for ten weeks shielded the neurons and NVU cells from ultrastructure remodeling.

Three deaths were noted in the AD-induced group in this investigation, compared to two in the curative group. It is important to evaluate mortality rates since prolonged injection of 100 mg of aluminum chloride for 6 weeks can have deadly effects. The high death rate at 100 mg/kg would eventually increase to 70% after six weeks, as reported by **Ali et al. [67].** The lethal dose (LD50), which is the concentration of a chemical that is fatal to 50% of experimental animals exposed to it, was significantly exceeded by the mortality rate of AlCl3. These findings suggested that AD continued to spread on its own even after the cause was eliminated. According to **Crowell et al. [68]**, patients with more advanced stages of AD had a proportionately higher chance of death. The risk of death was raised by the presence of comorbidities, such as diabetes mellitus, hypertension, coronary heart disease, and cerebrovascular illnesses. According to **Désesquelles et al. [69]**, the leading causes of death for individuals with AD are believed to be pneumonia and malnourishment.

EMP did not result in hypoglycemia, according to the current study's estimate of blood glucose levels. In terms of statistics, there was no noticeable difference between the EMP-treated (curative and ameliorative) and non-EMP-treated (control and AD-induced) groups. This outcome is in line with a prior study that found that EMP, by itself or in conjunction with other antidiabetic medications (metformin, sulphonylurea, or pioglitazone) does not cause severe hypoglycemia **[70].**

It is believed that this work treats AD in two phases: the preclinical phase, which occurs before the disease manifests, and the second phase, which occurs after the disease manifests. According to the phases of AD, the first administration of EMP plus aluminum chloride (ameliotaive group IIIa) is referred to as the pre-clinical phase, during which Aβ accumulates in the cortex without causing

neurological symptoms. On the other hand, the second phase of the disease (curative group IIIb) is defined as the administration of EMP 3 mg for an additional 8 weeks after 100 mg of AlCl3 for 8 weeks, since AD has already developed during the first administration of AlCl3 alone. Mild cognitive impairment (MCI) characterizes this phase, where predementia symptoms are accompanied by tauopathy and neurodegeneration. The third stage of Alzheimer's disease (AD) is characterized by increasingly severe dementia symptoms as neurodegeneration irreversibly destroys neurons and neural circuits **[71].**

In this investigation, the Modified T-maze test was utilized to assess the central effect of EMP on rats' memory. The current study's results showed that simultaneous oral administration of 3 mg/kg EMP and 100 mg/kg AlCl3 for 8 weeks significantly improved spatial memory according to this test; in particular, the ameliorative group (IIIa) showed a significant increase in T maze score in comparison to other groups. Similarly, oral administration of 3 mg/kg EMP for 8 weeks following an initial 8 weeks of 100 mg/kg AlCl3 for the curative group IIIb produced a modest improvement in spatial memory, as indicated by the Modified T maze score. Statistically, group IIIb, the curative group, had a slightly higher T maze score than the AD-induced group. Corresponding to these findings, **Lin et al. [72]** suggested that the elevated cerebral levels of brain-derived neurotrophic factor (BDNF) in diabetic mice were responsible for the memory-enhancing impact of EMP. BDNF contributes to neuronal survival, development, and plasticity in addition to neurotransmission modulation. It is crucial to the processes of memory and learning **[73].**

Arafa et al. [74] found that one SGLT2i drug, canagliflozin, helps with memory impairment. By increasing BDNF levels, EMP can directly serve as a neuroprotective agent in AD **[6].**

In terms of the biochemical investigation, the ameliotaive group (IIIa) that received aluminum chloride and EMP concurrently showed a large drop in MDA levels and a high statistically significant increase in TAC when compared to the AD-induced group. Similar results were reported by **Ahmed et al. [75]**, who reported that EMP lowers biomarkers associated with oxidative stress.

A statistical study of the mean values of MDA in the brain tissue in the curative group (IIIb) of the current work revealed a statistically significant decrease as compared to the AD-induced group, while a statistically significant increase was observed in the TAC level. According to certain research, oxidative stress is reduced as a result of EMP's neuroprotective effects. EMP lowered MDA, improved catalase activity, and raised the amount of glutathione (GSH) in brain tissue. Furthermore, as per **Iannantuoni et al. [76] and Wiciński et al. [77]**, EMP decreased the production of mitochondrial superoxide in diabetic patients with heightened antioxidant defenses and concurrently demonstrated an elevation in the anti-inflammatory cytokine IL-10 following a 24-week empagliflozin treatment.

In the present investigation, light microscopic analysis of H&E-stained parasagittal slices from the hippocampal CA1 region and DG of ameliorative group IIIa of adult male albino rats showed a significant improvement in comparison to the AD-induced group. There was a clear decrease in the number of degraded cells, but many neuroglial cells were seen. The microscopic findings were confirmed by the current morphometric study, which revealed a highly significant increase in the thickness of the pyramidal and granular cell layers in the ameliorative group, group IIIa, when compared to the AD-induced group. Similar findings that EMP reduces histological alterations in brain tissue were corroborated by **Amin et al. [78].** However, when compared to the AD-induced group, light microscopic analysis of the H&E-stained of the curative group IIIb showed only modest improvement. The microscopic findings were confirmed by morphometric analysis, which revealed a considerable increase in the thickness of the pyramidal and granular cell layers in the curative group IIIb as compared to the AD-induced group. It made an effort to realign the layer structures in DG and CA1, while there was still noticeable distortion, with few pyramidal and granular cells showing reduced degeneration.

TEM showed varying improvements in the alterations in hippocampal alternation. Pyramidal cells with euchromatic oval nuclei and prominent nucleoli were found in ameliorative group IIIa. Free ribosomes and rough endoplasmic reticulum were present in the surrounding cytoplasm. Oval euchromatic nuclei and large nucleoli were present in pyramidal cells in the curative group IIIb. There was evidence of nuclear clefting, or nuclear envelope invagination. There were dilated rER and seemingly normal mitochondria in the surrounding cytoplasm. These results, which show that EMP has

a neuroprotective impact by reducing cell necrosis and apoptosis due to suppression of many pathways that induce cerebral tissue damage and neuronal death, were elucidated **by Al Mudhafar et al. [79].** Furthermore, pro-inflammatory and oxidative stress markers can be decreased by EMP. Additionally, cerebral ischemia/reperfusion (I/R) injury is declined by this mechanism **[78].**

EMP increases the respiratory capacity of mitochondria, according to **Seefeldt et al. [80]**. The treatment of EMP-Chronic also altered myocardial metabolism and enhanced mitochondrial fatty acid oxidation. In order for EMP to shrink the myocardium's infract region. Given that neurons are subject to fluctuations in bioenergetics, mitochondrial activity is essential for preserving the homeostasis of neurons. As we have discussed, a key factor in the pathophysiology of Alzheimer's disease pathology is mitochondrial malfunction **[81]. Abdel-Latif et al. [82]** administered low and high concentrations of EMP to rats. Rats in a carotid artery blockage ischemia paradigm exhibited less neurological deficits. Notably, higher neurological scores were displayed by those receiving higher dosages of EMP, indicating that the drug's beneficial effects were dose-dependent. EMP reduced the synthesis of caspase-3, decreased the infarct extent, and increased the expression of vascular endothelial growth factor A and the level of hypoxia-inducible factor 1α (HIF-1α) in contrast to the control group.

TEM of the curative group's pyramidal cells had a large, irregular nuclear membrane that invaginated the nucleus to form the nuclear reticulum. This could account for the fact that a number of earlier studies generally depicted the nucleus as a smooth, spherical structure surrounded by the inner and outer membranes of the nuclear envelope and supported by an internal filamentous protein meshwork known as the nucleoskeleton of Lamin. For highly condensed heterochromatic DNA to be attached to the nuclear membrane, the lamin nucleoskeleton forms a filamentous meshwork **[83].** According to **Frost et al. [84],** heterochromatic DNA relaxation is a cellular outcome of lamin dysfunction in laminopathies. They also showed that acquired lamin misregulation due to aberrant cytoskeletal-nucleoskeletal interaction amplifies heterochromatin relaxation and neuronal death in an in vivo model of neurodegenerative tauopathy. **Frost et al. [84],** added that individuals with AD experience nucleoplasmic reticulum enlargement due to Tau-induced reduction of Lamin protein levels. Nuclei involve tubular invasions of the nuclear membrane known as the "nucleoplasmic reticulum" in certain cell types and pathological conditions, according to **Cornelison et al. [85].** Nucleoplasmic reticulum enlargement has recently been found to play a part in mediating neurodegeneration in tauopathies, like AD. In this work, light microscopic analysis of DG revealed that many immature neurons' small oval nuclei were seen in the subgranular zone (SGZ), with the number of viable mature GC neurons in ameliorative group IIIa rising. This was verified by morphometric analysis, which showed a notable increase in the GC layer's thickness. This could be explained by the BDNF signaling cascades that induce neurogenesis in the DG of the hippocampal region, stimulating the proliferation and differentiation of immature cells into progenitor cells and mature granular neurons **[86].** On the other hand, a modest morphometric drop in GC layer thickness was noted in the curative group IIIb, along with a small number of immature nerve cells. This suggests that the differentiation of newly formed cells into progenitor cells and their proliferation have decreased. The enhanced light and electron microscopy analysis of group III could potentially clarify how EMP enhances antioxidant status by decreasing MDA, increasing catalase activity, and elevating glutathione (GSH) concentration in brain regions. By reducing the size of atherosclerotic plaques and acting as an anti-inflammatory, EMP also increases blood flow **[78].** Examining Congo red stained parasagittal sections from adult male albino rats' hippocampus CA1 area and DG of ameliorative group IIIa, which received early concomitant EMP with AlCl3, revealed that, in contrast to the AD-induced group, there was no red coloration in any of the three layers or in the blood vessels, and DG was free of any red coloration caused by amyloid deposits. **Jadhav and Kulkarni [29]** obtained comparable results in the hippocampus and cortex. Conversely, the therapeutic group IIIb showed sparse focal red deposits remained inside blood vessels in CA1 and densely positive red foci in DG, despite receiving late EMP after 8 weeks of AlCl3 treatment. These findings corroborated those of **Khan et al. [87],** who noted a small amount of amyloid deposits in the group receiving EMP treatment in the hyperglycemic induced paradigm. In order to explain this result, **Khan et al. [87]** added that EMP improves oxidative stress and mechanisms independent of glycemic control, such as reduced

levels of important inflammatory biomarkers (tau protein, tau protein, TNF-α, IL-6, and IL-1β). As a result, EMP can limit tau phosphorylation by reducing the amounts of neural proteins, specifically Aβ40 and Aβ42, tau protein, and Glycogen synthase kinase-3 (GSK-3β).

Amyloid pathology may be lessened by EMP's anti-inflammatory and oxidative stress-reduction capabilities. According to **Nigam et al. [88]**, the effect of BDNF reinforced these findings by promoting non-amyloidogenic APP processing. According to their research, APP is degraded by an enhanced α-secretase pathway, which is how both BDNF and exercise reduce the production of harmful Aβ peptides. This anti-amyloidogenic APP processing involves subcellular translocation of α-secretase and a rise in intracellular neuroprotective APP peptides that can bind and block β-secretase.Another way that EMP improves cognitive function is through its anti-atherosclerotic action. EMP restricts the amount of atherosclerotic plaque in the aortic arch and valve, as demonstrated by **Han et al. [8].** SGLT2i dramatically lowers mortality and cardiovascular disease. Because SGLT2i improves endothelial dysfunction, lowers oxidative stress and vascular inflammation, it has an anti-atherosclerotic effect **[89].**

In the current study, GFAP immunostaining was examined under a light microscope in immunohistochemically stained sections from ameliorative group IIIa. This examination revealed a mild increase in the positive immunoreaction for GFAP within the cell bodies and their processes in CA1 and DG astrocytes. Additionally, statistical analysis revealed a mild increase in the mean value of the in the area percent of GFAP immunoreaction in comparison to other groups. Conversely, within the cell bodies and processes of the astrocytes in curative group IIIb, there was a moderats rise in the positive immunoreaction for GFAP. A moderate rise in the mean value of the area percent of GFAP of immunoreaction was seen in CA1 and DG when compared to other groups, as supported by statistical analysis. Similar results were reported by **Alhakamy et al. [90],** who proposed that treatment with Empagliflozin nanoemulsion (EMP-NE) led to a significant decrease in the expression levels of GFAP and IBA-1 molecule. This suggests that astrogliosis has significantly decreased. **Hayden et al. [66]** indicated that EMP used a neuroprotective impact on neurovascular remodeling, which includes loss of endothelium integrity, thickening of the basement membrane, disruption of astrocytes and pericytes, and loss of myelin and neurons. These findings are consistent with the current findings. EMP was found to have anti-inflammatory properties by reducing the expression of tumor necrosis factor α, interleukin 6, monocyte chemo attractant protein 1, serum amyloid A, and inflammatory cell infiltration, according to **Al Hamed and Elewa [91].** According to **Shim et al. [92]**, astrocytes exhibit a significant de novo increase of SGLT2. Furthermore, perivascular structures that were positive for GFAP showed a significant expression of SGLT2, which is in line with perivascular astrocyte end foot. TEM displayed in ameliorative group IIIa, aggregates of adjacent neuroglial cells; elongated nucleus of microglia, electron dense indented nucleus of astrocyte, and another cell with electron lucent indented nucleus mostly different stages of astrocytes. In acute ischemic stroke, canagliflozin has a beneficial effect on post-ischemic brain edema and decreases astrocyte swelling.

The morphometric analysis corroborated the light microscopic observation of a notable increase in SYP immunoreactivity on the surface of pyramidal cells and their apical dendrites, as well as the surface of granule cell bodies with their apical dendrites, in sections from ameliorative group IIIa that had been immunohistochemically stained. Comparing ameliorative group IIIa to other groups, statistical analysis revealed a significant increase in the mean value of the optical density of (SYP) immunoreaction. In contrast, curative group IIIb demonstrated a mild increase in (SYP) immunoreactivity on the surface of granule cell bodies, pyramidal cells, and their apical dendrites. According to a statistical analysis of the morphometric investigation, there was a considerable rise in the optical density of (SYP) when compared to the AD-induced group, but a slight increase in the mean value of the optical density of (SYP) immunoreaction in the curative group IIIb compared to the other groups. According to **Edelmann et al. [93]**, BDNF influences dendritic spines and acts on pre- and post-synaptic locations, hence serving as a major mediator of neuronal plasticity within the central nervous system. TEM confirmed our results when detected improvement in oligodentrocytes and myelin sheath of nerve axons**,** in amelioreative group IIIa showed oligodendroglia cell with irregular euchromatic nucleus and multiple nerve axons with intact myelin sheath.

Conclusion and recommendations:

The results of this study showed that AD caused by aluminum chloride caused biochemical and histological degenerative changes in the hippocampus CA1 and DG. While early management with EMP may have a more ameliorative effect than late curative measures, this was confirmed structurally, biochemically, and statistically. Antioxidant, anti-inflammatory, and anti-atherosclerotic activities with vascular protection mediate the neuroprotective action of EMP. EMP lowers Aβ levels, improves insulin resistance, and increases BDNF synthesis. Finally, regardless of the glucose scenario, EMP may have significant protective effects in AD. Because EMP has been shown to produce greater benefits than late acting therapies, it is advised to utilize it as soon as possible to treat tissue injuries brought on by AD degenerative lesions. The effectiveness of EMP with AD should be further studied, and more research is needed to completely understand the processes and long-term effects of using it for purposes other than diabetes. It ought to be advising EMP in AD patients' clinical studies.

Conflict of interest

The authors declare that there is no conflict of interest.

Funding

The authors declare that they did not receive funding.

REFERENCES

1. Samanta S, Ramesh M and Govindaraju T. Alzheimer's Disease: Recent Findings in Pathophysiology, Diagnostic and Therapeutic Modalities, ch. 1, pp. 1-34. Chem Sci. 2022.
2. Duchesne S, Rousseau LS, Belzile F, Welsh LA, Cournoyer B, Arseneau M, et al. a scoping review of alzheimers disease hypotheses: the case for a multi-factorial theory. MedRxiv, 2023; 2023-07.
3. Sharma K, Pradhan S, Duffy LK, Yeasmin S, Bhattarai N and Schulte MK. Role of Receptors in Relation to Plaques and Tangles in Alzheimer's Disease Pathology. Int. J. Mol. Sci., 2021; 22(23), 12987.
4. Lang M, Colby S, Ashby- Padial C, Bapna M, Jaimes C, Rincon SP et al. An imaging review of the hippocampus and its common pathologies. J Neuroimaging, 2024; 34(1), 5-25.
5. Frampton JE. Empagliflozin: a review in type 2 diabetes. Drugs, 2018; 78, 1037-1048.
6. Pawlos A, Broncel M, Woźniak E and Gorzelak-Pabiś P. Neuroprotective Effect of SGLT2 Inhibitors. Mol., 2021; 26(23), 7213.
7. Tharmaraja T, Ho JS, Sia CH, Lim NA, Chong YF, Lim AY, et al. Sodium-glucose cotransporter 2 inhibitors and neurological disorders: A scoping review. THER ADV CHRONIC DIS, 2022; 13.
8. Han JH, Oh TJ, Lee G, Maeng HJ, Lee DH, Kim KM, et al. The beneficial effects of empagliflozin, an SGLT2 inhibitor, on atherosclerosis in ApoE $^{-/-}$ mice fed a western diet. Diabetologia, 2017; 60(2), 364–76.
9. Singh NA, Bhardwaj V, Ravi C, Ramesh N, Mandal KA and Khan ZA. EGCG Nanoparticles Attenuate Aluminum Chloride Induced Neurobehavioral Deficits, Beta Amyloid and Tau Pathology in a Rat Model of Alzheimer's Disease. Front. aging neurosci., 2018; 10, 244.
10. Deacon RM and Rawlins JN. T-maze alternation in the rodent. Nat. Protoc., 2006; 1(1), 7–12.
11. Ahmadi-Noorbakhsh S, Farajli Abbasi M, Ghasemi M, Bayat G, Davoodian N, Sharif-Paghaleh E, et al. Anesthesia and analgesia for common research models of adult mice. Lab. Anim. Res., 2022; 38(1), 40.
12. Kabasakalian P, Kalliney S and Westcott A. Enzymatic blood glucose determination by colorimetry of N, N-diethylaniline-4-aminoantipyrine. Clin. Chem., 1974; 20(5), 606-7.
13. Ohkawa H, Ohishi N and Yagi K. Assay for lipid peroxides in animal tissues by thiobarbituric acid reaction. Anal. Biochem., 1979; 95(2), 351-8.
14. Koracevic D, Koracevic G, Djordjevic V, Andrejevic S and Cosic V. Method for the measurement of antioxidant activity in human fluids. J. Clin. Pathol., 2001; 54(5), 356-61.
15. Suvarna SK, Layton C and Bancroft JD. Theory and practice of histological techniques, eighth edition. J Res Health Sci, 2018; (pp. 69-87), 239-41.
16. Das D, Paul A, Maity SK, Chatterjee S and Chakrabarti P. Subcutaneous amyloidoma models for screening potential anti-fibrillating agents in vivo. STAR protocols, 2021; 2(4).
17. Kim SW, Roh J and Park CS. Immunohistochemistry for pathologists: protocols, pitfalls, and tips. J Pathol Transl Med., 2016; 50(6), 411-8.
18. Mukhiya GW, Mukhiya GK and Bansal KK. Role of glial fibrillary acidic protein (GFAP) marker in central nervous system lesions. Indian J Pathol Oncol, 2017; 4, 465-7.
19. Tampellini D, Capetillo-Zarate E, Dumont M, Huang Z, Yu F, Lin MT, et al. Effects of synaptic modulation on β-amyloid, synaptophysin, and memory performance in Alzheimer's disease

transgenic mice. J. Neurosci., 2010; 30(43), 14299-304.

20. Jurga AM, Paleczna M, Kadluczka J and Kuter KZ. Beyond the GFAP-astrocyte protein markers in the brain. Biomol., 2021; 11(9), 1361.

21. El-Adli D, Gawish SA, AbdElFattah AM, Soliman MF. The effect of experimentally-induced diabetes on rat hippocampus and the potential neuroprotective effect of Cerebrolysin combined with insulin. A histological and immunohistochemical study. Egypt. j. basic appl. sci., 2023; 10(1), 255-73.

22. Tizro P, Choi C and Khanlou N. Sample preparation for transmission electron microscopy. Biobanking: methods and protocols, 2019; 417-424

23. Spijker S. Dissection of rodent brain regions. Neuroproteomics, 2011; 13-26.

24. Hayat M. Principles and techniques of electron microscopy, biological applications. Cambridge: Cambridge University Press. 2000; 543 p.

25. Davis KE, Burnett K, Gigg J. Water and T-maze protocols are equally efficient methods to assess spatial memory in 3xTg Alzheimer's disease mice. Behav. Brain Res., 2017; 331, 54-66.

26. Chen X, Zhang M, Ahmed M, Surapaneni KM, Veeraraghavan VP and Arulselvan P. Neuroprotective effects of ononin against the aluminium chloride-induced Alzheimer's disease in rats. Saudi J. Biol. Sci., 2021; 28(8), 4232-9.

27. Dharmajaya R and Sari DK. Malondialdehyde value as radical oxidative marker and endogenous antioxidant value analysis in brain tumor. Ann. med. surg., 2022; 77.

28. Skalny AV, Aschner M, Jiang Y, Gluhcheva YG, Tizabi Y, Lobinski R, et al. Molecular mechanisms of aluminum neurotoxicity: Update on adverse effects and therapeutic strategies. In Advances in Neurotoxicology . AP. 2021; (5), (pp. 1-34).

29. Jadhav R and Kulkarni YA. Neuroprotective effect of Quercetin and Memantine against AlCl3-Induced neurotoxicity in albino Wistar rats. Mol., 2023; 28(1), 417.

30. Li J, Zhang DD, Wang CQ, Shi M and Wang LL. Protective effects of low-intensity pulsed ultrasound on aluminum overload-induced cerebral damage through epigenetic regulation of brain-derived neurotrophic factor expression. Biosci. Rep., 2019; 39(1).

31. Lakshmi VS, Sudhakar M and Prakash KS. Protective effect of selenium against aluminum chloride-induced Alzheimer's disease: behavioral and biochemical alterations in rats. Biol. Trace Elem. Res., 2015; 165, 67-74.

32. Gazia MA. The possible protective effect of Gardenia Jasminoides extracts on the dentate gyrus changes in an Alzheimer-induced model in adult male albino rats: Histological and Immunohistochemical study. Egypt. J. Histol., 2019; 42(2), 393-407.

33. Gao C, Liu Y, Jiang Y, Ding J and Li L. Geniposide Ameliorates Learning Memory Deficits, Reduces Tau Phosphorylation and Decreases Apoptosis via GSK 3β Pathway in Streptozotocin- Induced A Alzheimer Rat Model. Brain Pathol., 2014; 24(3), 261-9.

34. Kumar A, Prakash A and Dogra S. Neuroprotective effect of carvedilol against aluminum induced toxicity: possible behavioral and biochemical alterations in rats. PR, 2011; 63(4), 915–23.

35. Maya S, Prakash T, Madhu KD and Goli D. Multifaceted effects of aluminium in neurodegenerative diseases: A review. BIOMED PHARMACOTHER, 2016; 83, 746-54.

36. Love S, Louis D and Ellison DW. Greenfield's Neuropathology. Eighth Edition ,CRC Press. 2008; (2)

37. Li B, Yamamori H, Tatebayashi Y, Shafit-Zagardo B, Tanimukai H, Chen S, et al. Failure of neuronal maturation in Alzheimer disease dentate gyrus. J. Neuropathol. Exp. Neurol., 2008; 67(1), 78-84.

38. Arredondo SB, Valenzuela-Bezanilla D, Mardones MD and Varela-Nallar L. Role of Wnt signaling in adult hippocampal neurogenesis in health and disease. Front. cell dev. biol., 2020; 8, 860.

39. Cioanca O, Hritcu L, Mihasan M and Hancianu M. Cognitive-enhancing and antioxidant activities of inhaled coriander volatile oil in amyloid β (1–42) rat model of Alzheimer's disease. Physiol. Behav., 2013; 120, 193-202.

40. Jankovska N, Olejar T and Matej R. Extracellular amyloid deposits in Alzheimer's and Creutzfeldt–Jakob disease: Similar behavior of different proteins? Int. J. Mol. Sci., 2020; 22(1), 7.

41. Ricchelli F, Drago D, Filippi B, Tognon G and Zatta P. Aluminum-triggered structural modifications and aggregation of β-amyloids. CMLS, 2005; 62, 1724-33.

42. Zaky A, Mohammad B, Moftah M, Kandeel KM and Bassiouny AR. Apurinic/apyrimidinic endonuclease 1 is a key modulator of aluminum-induced neuroinflammation. BMC Neurosci., 2013; 14, 26.

43. Exley C. Aluminium and iron, but neither copper nor zinc, are key to the precipitation of β-sheets of Aβ 42 in senile plaque cores in Alzheimer's disease. J. Alzheimer's Dis, 2006; 10(2-3), 173-7.

44. Bhattacharjee S, Zhao Y and Lukiw WJ. Deficits in the miRNA-34a-regulated endogenous TREM2 phagocytosis sensor-receptor in Alzheimer's disease (AD); an update. Front. aging neurosci., 2014; 6, 116.

45. Alexandrov PN, Zhao Y, Jones BM, Bhattacharjee S and Lukiw WJ. Expression of the phagocytosis-essential protein TREM2 is down-regulated by an aluminum-induced miRNA-34a in a murine microglial cell line. J. Inorg. Biochem., 2013; 128, 267-9.

46. Miyakawa T. Vascular pathology in Alzheimer's disease. Psychogeriatr., 2010; 10(1), 39-44.

47. Korte N, Nortley R and Attwell D. Cerebral blood flow decrease as an early pathological mechanism in Alzheimer's disease. Acta Neuropathol., 2020; 140(6), 793-810.

48. Kamar SA, Malak WA and Saad SA. Effect of caffeinated energy drinks on the structure of hippocampal cornu ammonis 1 and dentate gyrus of adult male albino rats. Anat Cell Biol., 2020; 53(3), 330.

49. Desai MK, Sudol KL, Janelsins MC, Mastrangelo MA, Frazer ME and Bowers WJ. Triple- transgenic Alzheimer's disease mice exhibit region- specific abnormalities in brain myelination patterns prior to appearance of amyloid and tau pathology. Glia, 2009; 57(1), 54-65.

50. El Hajj H, Savage JC, Bisht K, Parent M, Vallières L, Rivest S, et al. Ultrastructural evidence of microglial heterogeneity in Alzheimer's disease amyloid pathology. J. Neuroinflammation, 2019; 16, 1-19.

51. Serrano-Pozo A, Frosch MP, Masliah E and Hyman BT. Neuropathological alterations in Alzheimer disease. Cold Spring Harb Perspect Med, 2011; 1(1).

52. Cao Z, Yang X, Zhang H, Wang H, Huang W, Xu F, et al. Aluminum chloride induces neuroinflammation, loss of neuronal dendritic spine and cognition impairment in developing rat. Chemosphere, 2016; 151, 289-95.

53. Pathak D and Sriram K. Neuron-astrocyte omnidirectional signaling in neurological health and disease. Front. mol. neurosci., 2023; 16.

54. Pannese E. Neurocytology: fine structure of neurons, nerve processes, and neuroglial cells.2nd edition. Springer, 2015; p.319.

55. McConnell HL, Li Z, Woltjer RL and Mishra A. Astrocyte dysfunction and neurovascular impairment in neurological disorders: Correlation or causation? Neurochem. Int., 2019; 128, 70-84.

56. Lawrence JM, Schardien K, Wigdahl B and Nonnemacher MR. Roles of neuropathology-associated reactive astrocytes: a systematic review. Acta Neuropathol. Commun., 2023; 11(1), 42.

57. Rao YL, Ganaraja B, Murlimanju BV, Joy T, Krishnamurthy A and Agrawal A. Hippocampus and its involvement in Alzheimer's disease: a review.3 Biotech, 2022; 12(2), 55.

58. Kandimalla R, Vallamkondu J, Corgiat EB and Gill KD. Understanding Aspects of Aluminum Exposure in Alzheimer's disease Development. Brain Pathol. (Zurich, Switzerland), 2016; 26(2), 139–154.

59. Nahirney PC and Tremblay ME. Brain ultrastructure: putting the pieces together. Front. cell dev. biol., 2021; 9.

60. Lippa CF and Rosso AL. Loss of synaptophysin immunoexpression in primary progressive aphasia. Am J Alzheimers Dis Other Demen, 2012; 27(4), 250-3.

61. Taha M, Elazab ST, Badawy AM, Saati AA, Qusty NF and Al-Kushi G. Activation of SIRT-1 Pathway by Nanoceria Sheds Light on Its Ameliorative Effect on Doxorubicin-Induced Cognitive Impairment (Chemobrain): Restraining Its Neuroinflammation, Synaptic Dysplasticity and Apoptosis. Pharm., 2022; 15(8): 918

62. Honer WG. Pathology of presynaptic proteins in Alzheimer's disease: more than simple loss of terminals. Neurobiol. Aging, 2003; 24(8): 1047-62.

63. Shamasundar NM, Rao TS, Naidu MD, Ravid R and Rao SJ. A new insight on Al-maltolate-treated aged rabbit as Alzheimer's animal model. Brain Res. Rev., 2006; 52(2), 275-92.

64. Walton JR. Brain lesions comprised of aluminum-rich cells that lack microtubules may be associated with the cognitive deficit of Alzheimer's disease. Neurotoxicology, 2009; 30(6), 1059-69.

65. Hayden MR. Type 2 diabetes mellitus increases the risk of late-onset Alzheimer's disease: ultrastructural remodeling of the neurovascular unit and diabetic gliopathy. Brain Sci., 2019; 9(10), 262.

66. Hayden MR, Grant DG, Aroor AR and DeMarco VG. Empagliflozin ameliorates type 2 diabetes-induced ultrastructural remodeling of the neurovascular unit and neuroglia in the female db/db mouse. Brain Sci., 2019; 9(3), 57.

67. Ali AA, Ahmed HI and Abu-Elfotuh K. Modeling stages mimic Alzheimer's disease induced by different doses of aluminum in rats: focus on progression of the disease in response to time. J Alzheimer's Parkinsonism Dementia, 2016; 1(1), 2.

68. Crowell V, Reyes A, Zhou SQ, Vassilaki M, Gsteiger S and Gustavsson A. Disease severity and mortality in Alzheimer's disease: an analysis using the U.S. National Alzheimer's Coordinating Center Uniform Data Set. BMC Neurol., 2023; 23(1), 302.

69. Désesquelles A, Demuru E, Salvatore MA, Pappagallo M, Frova L, Meslé F, et al. Mortality from Alzheimer's disease, Parkinson's disease, and dementias in France and Italy: a comparison using the multiple cause-of-death approach. J Nutr Health Aging, 2014; 26(2), 283-315.

70. Ndefo UA, Anidiobi NO, Basheer E and Eaton AT. Empagliflozin (Jardiance): A Novel SGLT2 Inhibitor for the Treatment of Type-2 Diabetes. P and T, 2015; 40(6), 364–8.

71. Sasaguri H, Nilsson P, Hashimoto S, Nagata K, Saito T, De Strooper B, et al. APP mouse models for Alzheimer's disease preclinical studies. EMBO J, 2017; 36(17), 2473–87.

72. Lin B, Koibuchi N, Hasegawa Y, Sueta D, Toyama K, Uekawa K, et al. Glycemic control with empagliflozin, a novel selective SGLT2 inhibitor, ameliorates cardiovascular injury and cognitive dysfunction in obese and type 2 diabetic mice. Cardiovasc. Diabetol., 2014; 13, 148.

73. Silakarma D and Sudewi AR. The role of brain-derivedneurotrophic factor (BDNF) in cognitive functions. Bali Med. J., 2019; 8(2), 518-25.

74. Arafa MS, Ali HA and Hassan MK. Canagliflozin prevents scopolamine-induced memory impairment in rats: Comparison with galantamine hydrobromide action. Chem Biol Interact, 2017; 277, 195–203.

75. Ahmed S, El-Sayed MM, Kandeil MA and Khalaf MM. Empagliflozin attenuates neurodegeneration through antioxidant, anti-inflammatory, and modulation of α-synuclein and Parkin levels in rotenone-induced Parkinson's disease in rats. SPJ, 2022; 30(6), 863–73.

76. Iannantuoni F, M de Marañon A, Diaz-Morales N, Falcon R, Bañuls C, Abad-Jimenez Z, et al. The SGLT2 Inhibitor Empagliflozin Ameliorates the Inflammatory Profile in Type 2 Diabetic Patients and Promotes an Antioxidant Response in Leukocytes. J. Clin. Med, 2019; 8(11), 1814.

77. Wiciński M, Wódkiewicz E, Górski K, Walczak M, Malinowski B. Perspective of SGLT2 Inhibition in Treatment of Conditions Connected to Neuronal Loss: Focus on Alzheimer's Disease and Ischemia-Related Brain Injury. Pharm., 2020; 13(11), 379.

78. Amin EF, Rifaai RA and Abdel- latif RG. Empagliflozin attenuates transient cerebral ischemia/reperfusion injury in hyperglycemic rats via repressing oxidative–inflammatory–apoptotic pathway. Fundam Clin Pharmacol, 2020; 34(5), 548-58.

79. Al Mudhafar AM, Abed FN, Abosaooda M, Al-Mudhafar RH, Hadi NR. Neuroprotective effect of empagliflozinon cerebral ischemia/reperfusion injury in rat model. Ann Rom Soc Cell Biol, 2021; 4876-87.

80. Seefeldt JM, Lassen TR, Hjortbak MV, Jespersen NR, Kvist F, Hansen J, et al. Cardioprotective effects of empagliflozin after ischemia and reperfusion in rats. Sci. Rep., 2021; 11(1), 9544.

81. Ashleigh T, Swerdlow RH and Beal MF. The role of mitochondrial dysfunction in Alzheimer's disease pathogenesis. Alzheimers Dement, 2023; 19(1), 333-42.

82. Abdel-Latif RG, Rifaai RA and Amin EF. Empagliflozin alleviates neuronal apoptosis induced by cerebral ischemia/reperfusion injury through HIF-1α/VEGF signaling pathway. Arch. Pharmacal Res., 2020; 43(5), 514–25.

83. Camozzi D, Capanni C, Cenni V, Mattioli E, Columbaro M, Squarzoni S, et al. Diverse lamin-dependent mechanisms interact to control chromatin dynamics. Focus on laminopathies. Nucleus (Austin, Tex.), 2014; 5(5), 427–40.

84. Frost B, Bardai FH and Feany MB. Lamin Dysfunction Mediates Neurodegeneration in Tauopathies. CB, 2016; 26(1), 129–36.

85. Cornelison GL, Levy SA, Jenson T and Frost B. Tau- induced nuclear envelope invagination causes a toxic accumulation of mRNA in Drosophila. Aging Cell, 2019; 18(1).

86. Oh JM, Jeong JH, Park SY and Chun S. Ginsenoside Compound K Induces Adult Hippocampal Proliferation and Survival of Newly Generated Cells in Young and Elderly Mice. Biomol., 2020; 10(3), 484.

87. Khan T, Khan S, Akhtar M, Ali J and Najmi AK. Empagliflozin nanoparticles attenuates type2 diabetes induced cognitive impairment via oxidative stress and inflammatory pathway in high fructose diet induced hyperglycemic mice. Neurochem. Int., 2021; 150.

88. Nigam SM, Xu S, Kritikou JS, Marosi K, Brodin L and Mattson MP. Exercise and BDNF reduce Aβ production by enhancing α- secretase processing of APP. J. Neurochem.y, 2017; 142(2), 286-96.

89. Scisciola L, Cataldo V, Taktaz F, Fontanella RA, Pesapane A, Ghosh P, et al. Anti-inflammatory role of SGLT2 inhibitors as part of their anti-atherosclerotic activity: Data from basic science and clinical trials. Front. cardiovasc. med., 2022; 9.

90. Alhakamy NA, Aljehani EA, Abdel-Naim AB, Shaik RA, Iqubal MK, Asfour HZ, et al. Development, optimization, and evaluation of Empagliflozin nanoemulsion for the management of neuroinflammation associated Alzheimer's disease. Int. J. Drug Deliv. Technol., 2024; 93, 105425.

91. Al Hamed FA and Elewa H. Potential therapeutic effects of sodium glucose-linked cotransporter 2 inhibitors in stroke. Clin. Ther, 2020; 42(11), e242-e9.

92. Shim B, Stokum JA, Moyer M, Tsymbalyuk N, Tsymbalyuk O, Keledjian K, et al. Canagliflozin, an Inhibitor of the Na+-Coupled D-Glucose Cotransporter, SGLT2, Inhibits Astrocyte Swelling and Brain Swelling in Cerebral Ischemia. Cells, 2023; 12(18), 2221.

93. Edelmann E, Leßmann V and Brigadski T. Pre-and postsynaptic twists in BDNF secretion and action in synaptic plasticity. Curr. Neuropharmacol, 2014; 76, 610-27.

Citation

Shaheen, M., Elshal, L., Mohamed, G., Reda, S. Possible Effects of Empagliflozin on Hippocampal Structural Changes Associated with Alzheimer's Disease Induced by Aluminum Chloride in Adult Male Albino Rats (Histological and Immunohistochemical Study). ***Zagazig University Medical Journal*****, 2024; (228-255): -. doi: 10.21608/zumj.2024.319646.3575**

Table 1s: demonstrates the mortality rates in different studied groups. The mortality rate in AD-induced group is more than curative group.

	Mortality rate *(%)*	
	N=6	*%*
Control	0	0 %
Alzheimer-induced	3	50 %
Ameliorative	0	0 %
Curative	2	33.3 %

Table 2s: demonstrates comparison between different control subgroups regarding the mean value of different parameters.

	T-Maze *Mean ± SE*	**MDA** *Mean ± SE*	**TAC** *Mean ± SE*
Control 1a	7.17 ± 0.4 ^{A}	1.33 ± 0.02^{A}	0.18 ± 0.007 ^{A}
Control 1b	7.5 ± 0.43 ^{A}	1.29 ± 0.01 ^{A}	0.18 ± 0.02 ^{A}
Control 1c	7 ± 0.37 ^{A}	1.28 ± 0.01 ^{A}	0.16 ± 0.003 ^{A}

-Data represented as (Mean ± SE)

-Within the same column, values without common superscript capital letters are significantly different ($p<0.05$)

Table 3s: representing comparison between different parameters regarding the mean value in different studied groups.

	T-Maze ***Mean ± SE***	**MDA** ***Mean ± SE***	**TAC** ***Mean ± SE***	**Blood glucose** ***Mean ± SE***
Control	**7.17 ± 0.4** ^{A}	**1.33 ± 0.02**^{A}	**0.18 ± 0.007** ^{A}	**116 ± 2.79**^{A}
Alzheimer-induced	**3.17 ± 0.31**^{B}	**2.06 ± 0.003**^{B}	**0.05 ± 0.02**^{B}	**107 ± 4.08**^{A}
Ameliorative	**6.33 ± 0.8** ^{A}	**1.51 ± 0.09** ^{A}	**0.16 ± 0.03**^{A}	**117 ± 2.64**^{A}
Curative	**4.83 ± 0.4** ^{B}	**1.9 ± 0.01** ^{B}	**0.09 ± 0.01**^{B}	**116 ± 2.97**^{A}

-Data represented as (Mean ± SE)

-Within the same column, values without common superscript capital letters are significantly different ($p<0.05$)

Table 4s: showing comparison between different studied groups regarding the mean value of pyramidal cell layer thickness of CA1 and granular cell layer thickness of DG.

	PCL thickness of CA1 (µm) *Mean ± SE*	**GCL thickness of DG (µm)** *Mean ± SE*
Control	43.2 ± 1.37^{A}	69.3 ± 1.69^{A}
Alzheimer-induced	25.6 ± 2.06^{B}	37.9 ± 2.65^{B}
Ameliorative	43.2 ± 1.76^{A}	60.2 ± 1.5^{A}
Curative	33.5 ± 0.51^{C}	50.5 ± 1.89^{C}

-Data represented as (Mean ± SE)

-Within the same column, values without common superscript capital letters are significantly different ($p<0.05$)

Table 5s: Comparisons of optical density of SYP in the different Studied groups of the hippocampus of CA1 and DG.

	CA1 SYP *Mean ± SE*	**DG SYP** *Mean ± SE*
Control	0.85 ± 0.01^{A}	0.81 ± 0.01^{A}
Alzheimer-induced	0.49 ± 0.03^{B}	0.32 ± 0.01^{B}
Ameliorative	0.78 ± 0.03^{A}	0.79 ± 0.03^{A}
Curative	0.67 ± 0.02^{C}	0.49 ± 0.03^{C}

-Data represented as (Mean ± SE)
-Within the same column, values without common superscript capital letters are significantly different ($p<0.05$)

Table 6s: showing comparison between different studied groups regarding the mean value of GFAP %area in CA1 and DG.

	GFAP CA1 Area % *Mean ± SE*	GFAP DG % Area *Mean ± SE*
Control	5.17 ± 0.18^{A}	3.78 ± 0.16^{A}
Alzheimer-induced	14.32 ± 0.44^{B}	15.12 ± 0.39^{B}
Ameliorative	5.99 ± 0.17^{A}	4.8 ± 0.15^{A}
Curative	11.34 ± 0.35^{C}	8.96 ± 0.38^{C}

-Data represented as (Mean ± SE)
-Within the same column, values without common superscript capital letters are significantly different ($p<0.05$)

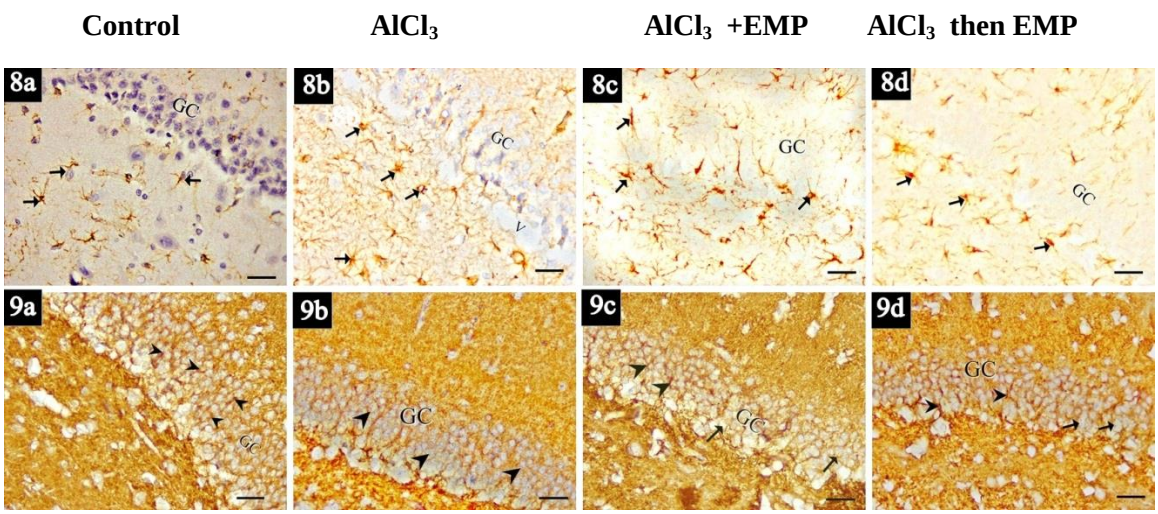

Plate. IVs:

Figure (8): photomicrograph of an immunohistochemical stained section in DG of the hippocampus for GFAP. positive immune reaction of GFAP in the cytoplasm of astrocyte and their processes in the form of brown coloration (arrows). Astrocytes are dispersed in between granular cell (GC) layer. (a) The control group showing positive immune reaction of GFAP and Few astrocytes are in between GC. (b) AD- induced group showing strong positive immune reaction for GFAP. Astrocytes appear larger in size with thick processes. Many astrocytes dispersed the layers of DG. Vacuolation(V) is also observed. (c) Ameliorative group showing mild positive immune reaction of GFAP. (d) Curative group showing moderate positive immune reaction of GFAP. Astrocytes appear large in size with multiple thick processes dispersed in between the gernular cell (GC) layer. Many astrocytes are seen dispersed among layers of DG. **(Immunoperoxidase reaction for GFAP, X400, scale bar20µm).**

Figure (9): photomicrograph of an immunohistochemical stained section in DG of the hippocampus for SYP. Positive reaction of SYP at the surface of granule cells in the granule cell layer (GC) in form of brown coarse beaded granules (arrow heads). (a) The control group shows strong positive reaction of SYP. (b) AD- induced group reveals marked decrease in the immunoreactivity of SYP in form of faint brown coloration (arrow heads) between granular cells (GC). (c) Ameliorative group showing marked increase in number of granular cells (GC) with immunoreactivity of SYP (arrow heads) while others still show weak positive immune-reactions (arrows). d) Curative group showing mild increase in immunoreactivity on the surface of the granular cell bodies (GC) (arrow heads). Other granular cells still display decrease in immunreactions (arrows). **(Immunoperoxidase reaction for SYP, X400, scale bar20µm).**

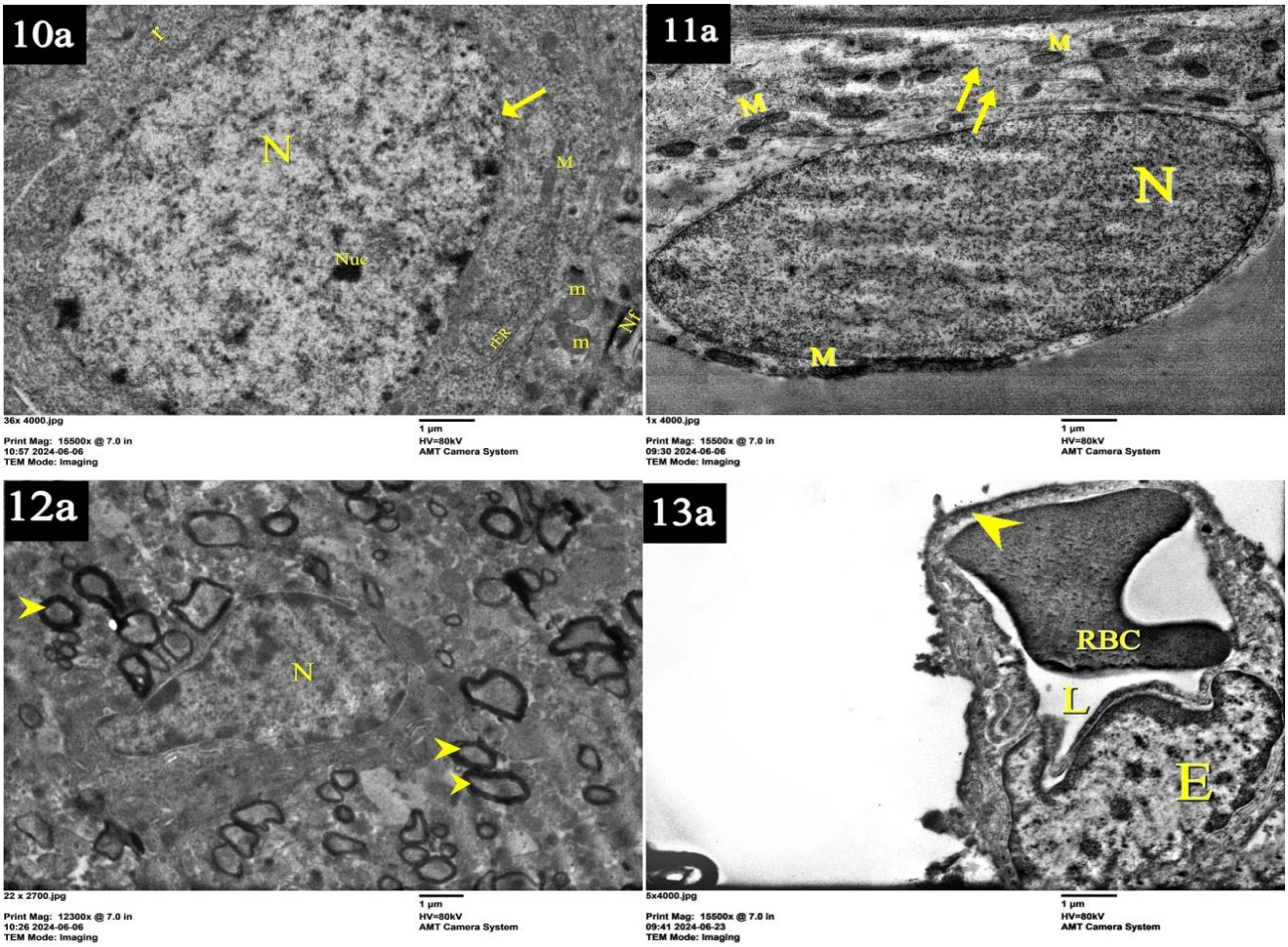

Plate.V. s: Showing electron Micrographs from part of hippocampus of **control group (a). Figure (10):** showing pyramidal cell with oval euchromatic nucleus (N), prominent nucleolus (Nuc) surround by a regular nuclear membrane (arrow). The cytoplasm contains Rod shaped mitochondria (M) and others spherical (m) are seen. Narrowing cisternae of rER, free ribosomes (r) and neurofilaments (Nf) appear **(TEM x 15500).**
Figure (11): Showing pyramidal cell with oval euchromatic nucleus (N). The surrounded cytoplasm containing multiple numerous mitochondria (M) with prominent cristae and microtubules (arrows) **(TEM x15500).**
Figure (12): reveals an oligodendroglia cell with euchromatic oval nucleus (N). The surrounding neuropil exhibits multiple nerve fibers surrounded by intact regular myelin sheaths (arrow heads) **(TEM x12300).**
Figure (13): showing the neurovascular unit consists of endothelial cell with flat euchromatic nucleus lining the capillary lumen which contains red blood corpuscle (RBC). Electron dense tight junction is observed (arrowhead) **(TEM x15500).**

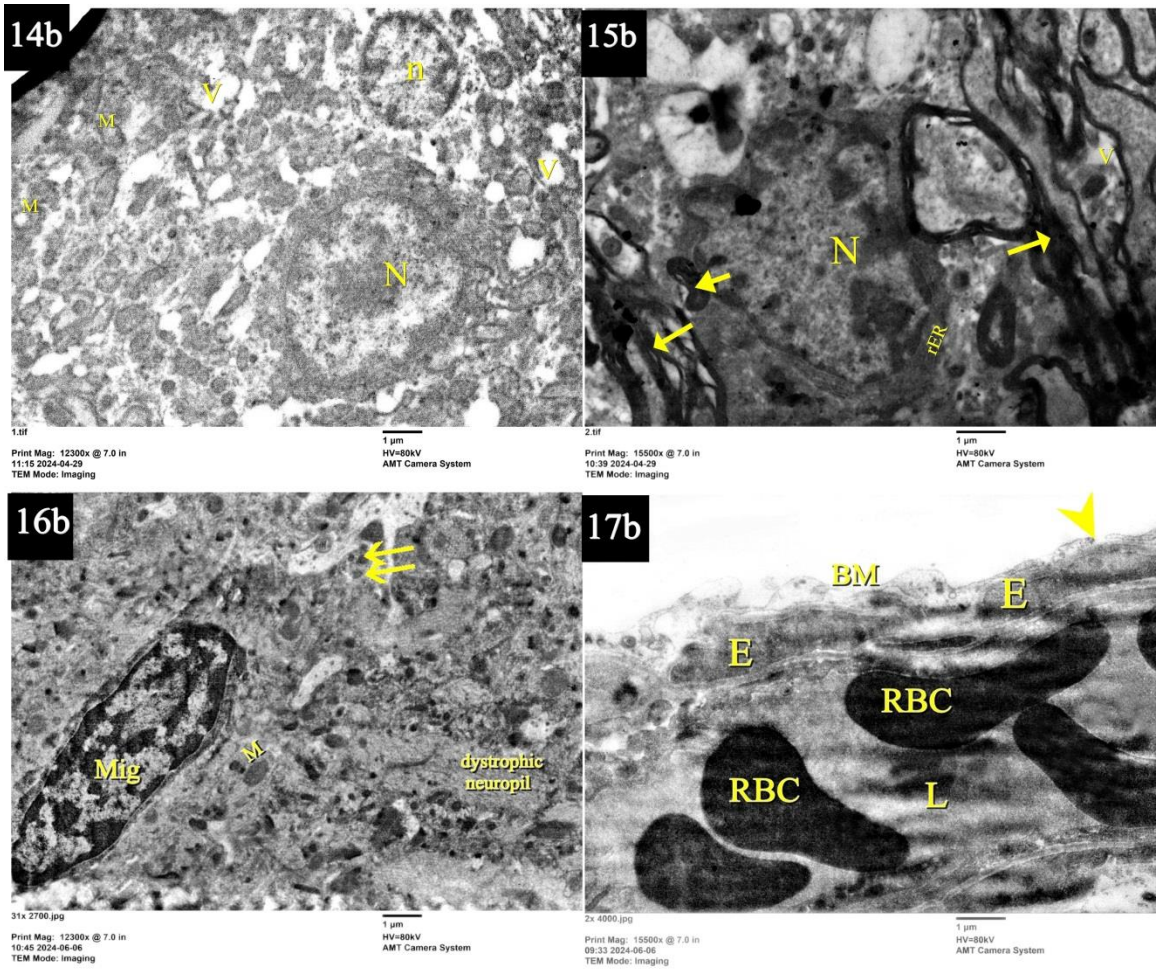

Plate.VI. s: Reveals electron Micrographs from part of hippocampus of **AD-induced group (b). Figure (14):** showing showing two adjacent pyramidal cells. One of them has shrunken nucleus (n). Another pyramidal cell has rounded heterochromatic nucleus (N). Numerous vacuoles (V) are dispersed in the disorganized neuropil. Mitochondria with destructed cristae (M) are observed **(TEM x 12300).**

Figure (15): reveals an oligodentrocyte with heterochromatic nucleus (N) and irregular nuclear membrane. The surrounding cytoplasm contains rough endoplasmic reticulum (rER), elongated dense vacuoles (thick arrow). Multiple nerve axons with irregular thick myelin sheath folding (arrows) and vacuolated axoplasms are seen (V) **(TEM x 15500).**

Figure (16): showing a microglial cell (mig) appears with elongated heterochromatic nucleus with peripheral chromatin condensation, the surrounding cytoplasm containing electron dense residual bodies (arrows) and swollen mitochondria (M) **(TEM x 12300).**

Figure (17): shows the neurovascular unit (NVU) consists of multiple endothelial cells (E) lining capillary lumen (L) which contains multiple (RBC), resting on apparently interrupted thick basement membrane (BM) (arrow head) **(TEM x 12300).**

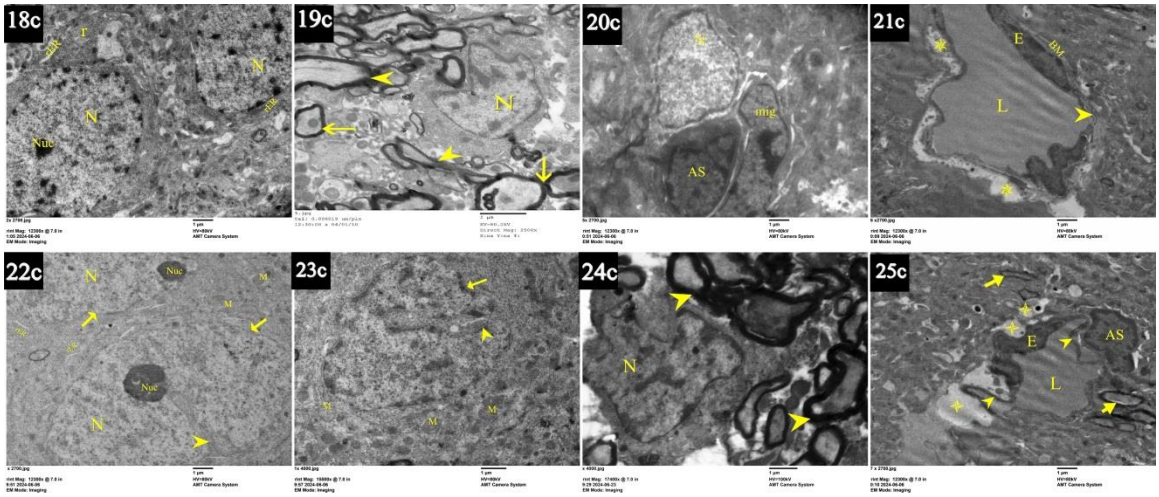

Plate.VII. s: Showing electron Micrographs from part of the hippocampus of EMP-treated groups (ameliorative and curative groups).

Amelioreative group (c). Figure (18): showing pyramidal cells with euchromatic oval nuclei (N) and prominent nucleoli (Nuc). The surrounding cytoplasm contains (rER) and free ribosomes (r) **(TEM x12300). Figure (19):** displays an oligodendroglia cell with irregular indented euchromatic nucleus (N). Nerve axons with regular myelin sheaths (arrows) and others with irregular myelin coats (arrowheads) are observed **(TEM x15500)**. **Figure (20):** showing aggregates of adjacent neuroglial cells; the elongated nucleus of microglia (mig), the electron-dense indented nucleus of astrocyte (AS), and another cell with electron-lucent indented nucleus (N) mostly different stages of astrocytes **(TEM x12300) . Figure (21):** showing the NVU consists of endothelial cells with electron-dense tight junction (arrowhead) between them. Intact BM is observed within NVU, and the capillary lumen (L) contains multiple (RBCs). Astrocyte endfeet (asterisk) appears as a thin clear zone bordered on BM **(TEM x12300).**

Curative group (d). Figure (22): showing two adjacent pyramidal cells with oval euchromatic nuclei and prominent nucleoli (Nuc) surrounded by an irregular nuclear membrane (arrows). Nuclear cleft (nuclear envelope invagination) is observed (head arrows). The surrounding cytoplasm contains mitochondria (M) and dilated rER.

(TEM x 12300).

Figure (23) reveals a pyramidal cell with an irregular and swollen nuclear membrane (arrow), which invaginates inside the nucleus, forming the nuclear reticulum (arrowhead). Swollen mitochondria (M) are observed. **(TEM x 15500). Figure (24):** displaying an oligodendroglia cell with an irregular euchromatic nucleus (N). Thick intact myelin coats of multiple nerve fibers (arrowheads) are seen **(TEM x 17400).**

Figure (25): showing NVU consists of heterochromatic endothelial cells (E) with electron-dense tight junction (arrow heads) lining capillary lumen (L). Astrocyte cell (AS) with a heterochromatic nucleus is adjacent to the capillary unit. Swollen astrocyte endfeet (asterisk) appears as a wide clear zone bordered on BM. Regular myelinated nerve axons (thick arrow) close to the capillary unit are observed, while others have disturbed myelin coat(arrow) **(TEM x 12300).**